J. Fluid Mech. (2002), *vol.* 455, *pp.* 21–62.
DOI: 10.1017/S0022112001007042 Printed in the United Kingdom

Shear flow of highly concentrated emulsions of deformable drops by numerical simulations

By ALEXANDER Z. ZINCHENKO
AND ROBERT H. DAVIS

Department of Chemical Engineering, University of Colorado,
Boulder, CO 80309-0424, USA
e-mail: zinchenk@colorado.edu; robert.davis@colorado.edu

(Received 23 April 2001 and in revised form 16 August 2001)

An efficient algorithm for hydrodynamical interaction of many deformable drops subject to shear flow at small Reynolds numbers with triply periodic boundaries is developed. The algorithm, at each time step, is a hybrid of boundary-integral and economical multipole techniques, and scales practically linearly with the number of drops N in the range $N < 1000$, for $N_\triangle \sim 10^3$ boundary elements per drop. A new near-singularity subtraction in the double layer overcomes the divergence of velocity iterations at high drop volume fractions c and substantial viscosity ratio λ. Extensive long-time simulations for $N = 100$–200 and $N_\triangle = 1000$–2000 are performed up to $c = 0.55$ and drop-to-medium viscosity ratios up to $\lambda = 5$, to calculate the non-dimensional emulsion viscosity $\mu^* = \Sigma_{12}/(\mu_e\dot{\gamma})$, and the first $N_1 = (\Sigma_{11} - \Sigma_{22})/(\mu_e|\dot{\gamma}|)$ and second $N_2 = (\Sigma_{22} - \Sigma_{33})/(\mu_e|\dot{\gamma}|)$ normal stress differences, where $\dot{\gamma}$ is the shear rate, μ_e is the matrix viscosity, and Σ_{ij} is the average stress tensor. For $c = 0.45$ and 0.5, μ^* is a strong function of the capillary number $Ca = \mu_e|\dot{\gamma}|a/\sigma$ (where a is the non-deformed drop radius, and σ is the interfacial tension) for $Ca \ll 1$, so that most of the shear thinning occurs for nearly non-deformed drops. For $c = 0.55$ and $\lambda = 1$, however, the results suggest phase transition to a partially ordered state at $Ca \leqslant 0.05$, and μ^* becomes a weaker function of c and Ca; using $\lambda = 3$ delays phase transition to smaller Ca. A positive first normal stress difference, N_1, is a strong function of Ca; the second normal stress difference, N_2, is always negative and is a relatively weak function of Ca. It is found at $c = 0.5$ that small systems ($N \sim 10$) fail to predict the correct behaviour of the viscosity and can give particularly large errors for N_1, while larger systems $N \geqslant O(10^2)$ show very good convergence. For $N \sim 10^2$ and $N_\triangle \sim 10^3$, the present algorithm is two orders of magnitude faster than a standard boundary-integral code, which has made the calculations feasible.

1. Introduction

Emulsions, i.e. dispersions of one immiscible liquid in another liquid, arise in a wide range of applications, including food processing, oil recovery and transportation, and pharmaceutical manufacturing. For many years, progress in understanding emulsion rheology was mainly empirical and limited to conditions of particular experiments. However, it is important to understand, from first principles, how microstructural details affect emulsion rheology. Among the most important factors are drop volume fraction and drop deformation. Recent progress in computational methods and more

powerful computer resources have made possible the examination of the effects that these factors have on emulsion microstructure and rheology.

For a two-dimensional model, Pozrikidis & coworkers used a direct boundary-integral method with 25–50 drops to simulate spatially homogeneous shear flows (Li, Charles & Pozrikidis 1996; Charles & Pozrikidis 1998; Breyiannis & Pozrikidis 2000) and wall-bounded and channel flows (Zhou & Pozrikidis 1993, 1994; Li & Pozrikidis 2000) at moderate area fractions. In the three-dimensional case, Kennedy, Pozrikidis & Skalak (1994) calculated the deformation and rheological response of a single drop in a simple shear flow, to find the effective viscosity and normal stress differences in dilute emulsions and extend earlier work (Cox 1969; Frankel & Acrivos 1970) to finite deformations. Mo & Sangani (1994) calculated the viscosity of concentrated random static emulsions of spherical drops. Pozrikidis (1993) simulated shear flow of deformable drops in ordered, three-dimensional flow (one drop per periodic cell) at moderate volume fractions by a boundary-integral method; his study complements the earlier work of Sangani & Lu (1987) on the viscosity of ordered emulsions of spherical drops in a simple cubic array.

Loewenberg & Hinch (1996) were the first to dynamically simulate shear flow of more realistic, disordered spatially homogeneous emulsions of three-dimensional deformable drops. They implemented a direct point-to-point boundary-integral method, with $O(N^2N_\triangle^2)$ scaling (where N is the number of drops in a periodic cell, and $N_\triangle$ is the number of triangular boundary elements per drop), and used $N = 12$ drops with $N_\triangle = 320$ boundary elements per drop to calculate the effective emulsion viscosity and normal stress differences for up to 30% drop volume fractions. Using the same implementation, Loewenberg (1998) presented some additional calculations at 30% concentration and analysed the usefulness of the mean-field model for rheological properties and critical breakup conditions.

In the present work, we make the same physical assumptions (Stokes flow, constant temperature and surface tension, no surfactants, equi-sized drops, Newtonian drop and matrix fluids) as in the papers of Loewenberg & Hinch (1996) and Loewenberg (1998). Our focus is on the rheological properties of spatially homogeneous three-dimensional emulsions at very high drop volume fractions, up to 55%, in a wide range of capillary numbers Ca, including the practical but difficult case of drops with small deformations. Such information bridges the gap between moderately concentrated emulsions and foams and reveals a number of qualitatively new features absent at low concentrations. Using large systems ($N \geqslant O(10^2)$) is important at high concentrations, as is using fine surface discretizations ($N_\triangle \sim 10^3$), and a direct $O(N^2N_\triangle^2)$ boundary-integral method would not be a practical option for dynamical simulations in this case. Our approach is instead based on the recent algorithm of Zinchenko & Davis (2000, hereafter referred to as paper I) for multidrop sedimentation and is a hybrid of the boundary-integral and economical multipole techniques (Zinchenko 1994, 1998), with multipoles playing the major role. An additional challenge, however, is that the basic periodic cell must change with time in shear-flow simulations, and the present far-field calculation techniques are thus necessarily different from those in paper I.

In § 2, the boundary-integral formulation is described. In § 3, we offer a new near-singularity subtraction technique for double-layer boundary integrals, which was crucial to overcome the divergence of velocity iterations in our simulations at high concentrations and substantial viscosity contrast between the drops and the surrounding matrix, without a loss of efficiency. In § 4, the scheme adapted from paper I for multipole-accelerated calculation of boundary integrals is outlined, with a particular emphasis on the differences between the shear-flow and sedimentation

cases. Appendix A presents the passive mesh stabilization algorithm used to maintain the quality of drop triangulations in dynamical simulations. Techniques for dynamical calculations of the far-field parts of the boundary integrals (i.e. after subtracting off the nearest-image contributions from the periodic Green's function) are described in Appendices B, C, and D. The known solutions in the dilute limit (Kennedy *et al.* 1994) and for periodic emulsions of spherical drops at high concentrations (Sangani & Lu 1987) provide tests for our code in § 5.1. Results for the dynamics of random concentrated emulsions are presented in § 5.2. All calculations were performed on DEC 500au and DEC 600au (500 and 600 MHz) single-processor UNIX workstations, or on DELL Dimension Pentiums III (733 and 1000 MHz).

2. Boundary-integral formulation

Consider an infinite set of deformable drops of viscosity μ' freely suspended in a medium of viscosity $\mu_e = \mu'/\lambda$ and subject to a steady mean shear flow $\boldsymbol{u}^o_\infty(\boldsymbol{x}) = (\dot\gamma x_2, 0, 0)$, where $\dot\gamma > 0$ is the shear rate. An equivalent radius of non-deformed drops is a_o (assumed, for simplicity, to be the same for all drops) and the capillary number is $Ca = \mu_e \dot\gamma a_o/\sigma$, where σ is the constant interfacial tension. The drop system is obtained from the basic configuration of N drops with surface centroids $\boldsymbol{x}^c_1, \ldots, \boldsymbol{x}^c_N$ in the cell V by triply periodic continuation into the whole space with periods $\boldsymbol{e}_1$, $\boldsymbol{e}_2$, $\boldsymbol{e}_3$. Initially, at $t = 0$, vectors $\boldsymbol{e}_1$, $\boldsymbol{e}_2$, $\boldsymbol{e}_3$ form an orthonormal basis $\boldsymbol{e}^o_1$, $\boldsymbol{e}^o_2$, $\boldsymbol{e}^o_3$, and the periodic cell V is then a unit cube, if the cell side L is taken as a characteristic length. For $t > 0$, the periodic cell is deformed by the mean flow and repeats itself in a cyclic manner, so, without loss of generality,

$$\left.\begin{aligned} &\boldsymbol{e}_1 = \boldsymbol{e}^o_1, \quad \boldsymbol{e}_2 = \boldsymbol{e}^o_2 + \gamma \boldsymbol{e}_1, \quad \boldsymbol{e}_3 = \boldsymbol{e}^o_3, \\ &\gamma = \dot\gamma t - \left[\dot\gamma t + \tfrac{1}{2}\right] \in \left[-\tfrac{1}{2}, \tfrac{1}{2}\right), \end{aligned}\right\} \tag{2.1}$$

and $V = \{\xi^i \boldsymbol{e}_i, |\xi^i| \leqslant 1/2\}$ (figure 1). The fluid velocity is expressed as $\boldsymbol{u}(\boldsymbol{x}) = \boldsymbol{u}^o_\infty(\boldsymbol{x}) + \tilde{\boldsymbol{u}}(\boldsymbol{x})$, where $\tilde{\boldsymbol{u}}(\boldsymbol{x})$ is triply periodic and is assumed to have zero mean $\langle\tilde{\boldsymbol{u}}\rangle$ over V, without loss of generality. A system of boundary-integral equations for $\boldsymbol{u}(\boldsymbol{x})$ on drop surfaces $S_1, S_2, \ldots, S_N$ is facilitated through the use of the periodic non-dimensional Green functions $\mathbf{G}^{(k)}(\boldsymbol{x})$, $k = 1, 2, 3$ (e.g. Hasimoto 1959; see Appendix B for more details) and the corresponding stress tensors $\boldsymbol{\tau}^{(k)}(\boldsymbol{x})$. With the normalization used herein, the vectors $\mathbf{G}^{(k)}(\boldsymbol{x})$ and the corresponding pressures $q^{(k)}(\boldsymbol{x})$ satisfy

$$\nabla^2 \mathbf{G}^{(k)}(\boldsymbol{x}) - \nabla q^{(k)}(\boldsymbol{x}) = \nabla \cdot \boldsymbol{\tau}^{(k)}(\boldsymbol{x}) = \sum_{\boldsymbol{m}} \delta(\boldsymbol{x} - \boldsymbol{P}(\boldsymbol{m})) \boldsymbol{e}^o_k, \tag{2.2}$$

where the summation is over all the lattice points $\boldsymbol{P}(\boldsymbol{m}) = m_1\boldsymbol{e}_1 + m_2\boldsymbol{e}_2 + m_3\boldsymbol{e}_3$ with integer m_1, m_2, m_3. Unlike $\mathbf{G}^{(k)}(\boldsymbol{x})$, the pressure $q^{(k)}(\boldsymbol{x})$ and stress tensor

$$\boldsymbol{\tau}^{(k)} = -q^{(k)}\boldsymbol{I} + (\nabla + \nabla^T)\mathbf{G}^{(k)} \tag{2.3}$$

are linear plus periodic functions. With $\langle\tilde{\boldsymbol{u}}\rangle = 0$ and $\dot\gamma L$ as the velocity scale, the non-dimensional fluid velocity on the drop surfaces is uniquely determined by a system of non-dimensional boundary-integral equations:

$$u_k(\boldsymbol{y}) = \frac{2(\lambda - 1)}{\lambda + 1} \sum_{\beta=1}^{N} \int_{S_\beta} \boldsymbol{u}(\boldsymbol{x}) \cdot \boldsymbol{\tau}^{(k)}(\boldsymbol{x} - \boldsymbol{y}) \cdot \boldsymbol{n}(\boldsymbol{x}) \, \mathrm{d}S_x + F_k(\boldsymbol{y}), \quad k = 1, 2, 3. \tag{2.4}$$

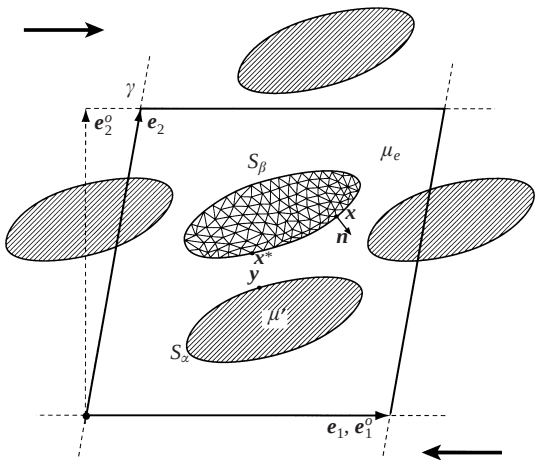

FIGURE 1. On the shear flow simulation with periodic boundaries. The periodic box V (contoured bold) is centred at the origin and is based on the lattice vectors $\boldsymbol{e}_1$, $\boldsymbol{e}_2$ and $\boldsymbol{e}_3$. The third dimension is not shown.

Here, the inhomogeneous term is

$$\boldsymbol{F}(\boldsymbol{y}) = \frac{2}{\lambda+1}\left[\boldsymbol{u}_\infty(\boldsymbol{y}) + \sum_{\beta=1}^{N}\frac{2a}{Ca}\int_{S_\beta}(k(\boldsymbol{x})-\langle k\rangle_\beta)\boldsymbol{n}(\boldsymbol{x})\cdot\boldsymbol{\mathsf{G}}(\boldsymbol{x}-\boldsymbol{y})\,\mathrm{d}S_{\boldsymbol{x}}\right], \tag{2.5}$$

where $\boldsymbol{u}_\infty(\boldsymbol{y}) = (y_2, 0, 0)$ is the non-dimensional mean flow, $a = a_o/L$ is the non-dimensional non-deformed radius, $k(\boldsymbol{x}) = (k_1+k_2)/2$ is the local mean of the principal surface curvatures, $\langle k\rangle_\beta$ is the average of k over S_β, $\boldsymbol{\mathsf{G}} = (\boldsymbol{\mathsf{G}}^{(1)}, \boldsymbol{\mathsf{G}}^{(2)}, \boldsymbol{\mathsf{G}}^{(3)})$ is the symmetric Green tensor, and $\boldsymbol{n}(\boldsymbol{x})$ is the outward unit normal at $\boldsymbol{x}\in S_\beta$. In (2.4) and in what follows (unless otherwise stated), indices 1, 2, 3 denote Cartesian vector and tensor components in the basis $\boldsymbol{e}_1^o$, $\boldsymbol{e}_2^o$, $\boldsymbol{e}_3^o$.

Wielandt's deflation (Kim & Karilla 1991; Pozrikidis 1992) could be applied to (2.4) to eliminate $\kappa = (\lambda-1)/(\lambda+1) = \pm 1$ from the spectrum of the boundary-integral operator. While this deflation was crucial in the analysis of two-bubble interactions (Zinchenko, Rother & Davis 1999), was widely used in two-dimensional rheological simulations (Charles & Pozrikidis 1998), and recommended in multidrop sedimentation (Zinchenko & Davis 2000), we found the deflation to offer almost no help in the present three-dimensional simulations at high concentrations with the viscosity ratio limited to $\lambda = 3$ or $\lambda = 5$. A probable explanation is a nearly continuous spectrum for the boundary-integral operator (2.4) at high drop volume fractions, so removal of the marginal eigenvalues only does not accelerate the convergence of iterations. More surprisingly, for large $\lambda \sim O(10)$, when iterations of (2.4) were often observed to diverge due to insufficient triangulations, the difficulty could not be eliminated by deflation. For the above reasons, the non-deflated form (2.4) was used in the present calculations. It is important, however, to reduce the variation of the integrands on drop surfaces in (2.4) (as done in (2.5)), in order to accelerate convergence in the multipole part (§4) of the algorithm; this goal is achieved by considering fluctuations $\boldsymbol{Q}(\boldsymbol{x})$ from the surface-averaged values:

$$\boldsymbol{Q}(\boldsymbol{x})|_{S_\beta} = \boldsymbol{u}(\boldsymbol{x}) - \langle\boldsymbol{u}\rangle_\beta, \quad \langle\boldsymbol{u}\rangle_\beta = \frac{1}{S_\beta}\int_{S_\beta}\boldsymbol{u}\,\mathrm{d}S. \tag{2.6}$$

Using the periodic kernel

$$\tilde{\boldsymbol{\tau}}^{(k)}(\boldsymbol{x}-\boldsymbol{y}) = \boldsymbol{\tau}^{(k)}(\boldsymbol{x}-\boldsymbol{y}) - (x-y)_k \boldsymbol{I},$$

instead of $\boldsymbol{\tau}^{(k)}$, (2.4) can be transformed to (cf. (2.12) of paper I)

$$\boldsymbol{u}(\boldsymbol{y}) = \frac{(\lambda-1)}{(\lambda+1)}\left[2\sum_{\beta=1}^{N}\int_{S_\beta}\boldsymbol{Q}(\boldsymbol{x})\cdot\tilde{\boldsymbol{\tau}}(\boldsymbol{x}-\boldsymbol{y})\cdot\boldsymbol{n}(\boldsymbol{x})\,\mathrm{d}S_{\boldsymbol{x}} + \langle\boldsymbol{u}\rangle_\alpha \right.$$
$$\left. + 2\sum_{\beta=1}^{N}\int_{S_\beta}(\boldsymbol{Q}\cdot\boldsymbol{n})\left(\boldsymbol{x}-\boldsymbol{x}_\beta^c\right)\mathrm{d}S_{\boldsymbol{x}}\right] + \boldsymbol{F}(\boldsymbol{y}), \quad \boldsymbol{y}\in S_\alpha \tag{2.7}$$

where the surface centroid is

$$\boldsymbol{x}_\beta^c = \frac{1}{S_\beta}\int_{S_\beta}\boldsymbol{x}\,\mathrm{d}S, \tag{2.8}$$

and the tensor $\tilde{\boldsymbol{\tau}} = \{\tau_{ij}^{(k)}\}$ is now symmetric in all three indices.

To solve (2.4) at each time step for $\lambda \neq 1$, the following version of the minimal residual technique is used. Having written (2.4) in the operator form $\boldsymbol{u} = \boldsymbol{B}\boldsymbol{u} + \boldsymbol{F}$, three simple iterations (if necessary) $\boldsymbol{u}_{i+1} = \boldsymbol{B}\boldsymbol{u}_i + \boldsymbol{F}$ $(i = 0, 1, 2)$ and corresponding residuals $\boldsymbol{r}_i = \boldsymbol{u}_{i+1} - \boldsymbol{u}_i$ are first calculated. The vector $\boldsymbol{u} = \lambda_1\boldsymbol{u}_1 + \lambda_2\boldsymbol{u}_2 + (1-\lambda_1-\lambda_2)\boldsymbol{u}_o$ is sought to minimize the L_2-norm of the residual

$$\boldsymbol{r}(\boldsymbol{u}) = \boldsymbol{B}\boldsymbol{u} + \boldsymbol{F} - \boldsymbol{u} = \lambda_1\boldsymbol{r}_1 + \lambda_2\boldsymbol{r}_2 + (1-\lambda_1-\lambda_2)\boldsymbol{r}_o, \tag{2.9}$$

$$\sum_{\alpha=1}^{N}\int_{S_\alpha}\boldsymbol{r}^2(\boldsymbol{u})\,\mathrm{d}S \to \min.$$

The parameters λ_1 and λ_2 are found from the solution of the corresponding 2×2 system, and the process can be continued, if necessary, using $\boldsymbol{u}$ and $\boldsymbol{u} + \boldsymbol{r}(\boldsymbol{u})$ as new $\boldsymbol{u}_o$ and $\boldsymbol{u}_1$, respectively. Iterations terminate once a residual in all boundary nodes on all drops is small compared to the average velocity variation on S_α:

$$\max|\boldsymbol{r}| < \delta\left[\sum_{\alpha=1}^{N}\int_{S_\alpha}\left[\boldsymbol{u}(\boldsymbol{x}) - \langle\boldsymbol{u}\rangle_\alpha\right]^2\mathrm{d}S \Big/ \sum_{\alpha=1}^{N}S_\alpha\right]^{1/2}, \tag{2.10}$$

with δ being typically 0.003; for a large number of drops, $\boldsymbol{u}(\boldsymbol{x}) - \langle\boldsymbol{u}\rangle_\alpha$ in (2.10) is a more appropriate velocity scale than $\boldsymbol{u}$. Upon convergence by (2.10), the average residual $|\boldsymbol{r}|$ over all nodes is typically 30–50 times smaller than $\max|\boldsymbol{r}|$. Using the minimum residual technique typically reduces the number of iterations by 30–40%, compared to simple iterations. These gains may be less than those from using biconjugate gradient iterations in boundary-integral calculations (Zinchenko, Rother & Davis 1997, 1999), but they do not require an adjoint operator (difficult to calculate for the combined boundary-integral–multipole scheme of § 4).

Drop surfaces are discretized by unstructured meshes with a fixed topology and updated by a Runge–Kutta time integration scheme, typically of second order, with a constant time step. The quality of surface triangulations is maintained during simulations by a version of passive mesh stabilization techniques (Zinchenko *et al.* 1997, 1999) outlined in Appendix A. Normals and curvatures are calculated in mesh nodes by the best paraboloid-spline (BPS) method of paper I; to expedite BPS calculations, a linear extrapolation from the two preceding time steps (with appropriate normalization) is used as an initial approximation for the normal vectors.

Unlike in our sedimentation calculations (paper I), artificial surface smoothing was not used in the present work. Due to the existence of the statistical steady state in shear flow, abnormal high curvatures $k \sim (20\text{–}25)a^{-1}$, which may occasionally develop in several (out of $O(10^5)$) nodes, tend to return back to normal. Without smoothing, our long-time runs (§ 5) had an extremely small probability of failure. In rare cases, when a high curvature developed on one drop (out of 100–200) which could cause instability, the drop was simply replaced by the three-dimensional ellipsoid of the largest possible volume which fits within the drop, to successfully continue the simulation; the effect of this procedure on the total drop volume fraction (less than 0.2–0.3% error) and viscometric functions was found to be negligible.

With $\mu_e\dot{\gamma}$ for the stress scale, the non-dimensional average stress tensor can be calculated as (e.g. Pozrikidis 2001)

$$\Sigma_{ij} = \text{I.T.} + \nabla_i (u_\infty)_j + \nabla_j (u_\infty)_i + \sum_{\alpha=1}^{N} \int_{S_\alpha} \left[\frac{2a}{Ca} \left(k(\boldsymbol{x}) - \langle k \rangle_\alpha \right) n_i \left(x - x_\alpha^c \right)_j + (\lambda - 1) \left(u_i n_j + u_j n_i \right) \right] \mathrm{d}S \tag{2.11}$$

(I.T. is an insignificant isotropic term) and characterized by the non-dimensional shear viscosity $\mu^* = \Sigma_{12} = \Sigma_{21}$ and non-dimensional normal stress differences $N_1 = \Sigma_{11} - \Sigma_{22}$ and $N_2 = \Sigma_{22} - \Sigma_{33}$. Note that our N_1, N_2 differ from N_1^P, N_2^P defined by Loewenberg (1998) by a factor of c/Ca, where c is the drop volume fraction. Using N_1, N_2 prevents loss of information in the spherical-drop limit $Ca \to 0$; likewise, the viscosity μ^*, rather than the particle shear stress $\Sigma_{12}^P = (\mu^* - 1)Ca/c$, is of interest at $Ca \to 0$.

3. Near-singularity subtractions

Success of the numerical solution of the boundary-integral equation (2.7) at high volume fractions and $\lambda \neq 1$, in particular the convergence of iterations, is crucially dependent on how accurately the double-layer integral (2.7) is represented in numerical implementations. In the exact formulation, (2.7) is known to have the characteristic values of $\kappa = (\lambda - 1)/(\lambda + 1)$ (i.e. the values for which (2.7) is degenerate) outside $(-1, 1)$, so simple iterations are convergent. In practice, however, simple iterations are often observed to diverge due to insufficient surface triangulations. Using advanced iterative schemes (minimal residual, etc.) does not help in this case, since a dynamical system with a distorted spectrum becomes close to degenerate at some instant of time, and the calculations crash. Since the kernel $\tilde{\boldsymbol{\tau}}(\boldsymbol{r}) \sim r^{-2}$ is strongly singular at $\boldsymbol{r} = \boldsymbol{x} - \boldsymbol{y} \to 0$, regularizations are needed, before the double layer can be approximated to a sufficient accuracy with a reasonable number of boundary elements. Consider the 'desingularization' for the integrals in (2.7),

$$2 \int_{S_\beta} \boldsymbol{Q}(\boldsymbol{x}) \cdot \boldsymbol{\tau}_o(\boldsymbol{x} - \boldsymbol{y}) \cdot \boldsymbol{n}(\boldsymbol{x}) \, \mathrm{d}S_x, \tag{3.1}$$

when the kernel is the free-space stresslet

$$\boldsymbol{\tau}_o(\boldsymbol{r}) = \frac{3}{4\pi} \frac{\boldsymbol{rrr}}{r^5} \tag{3.2}$$

(the general case (2.7) is discussed in § 4). When $\boldsymbol{y} \in S_\beta$, (3.1) is regularized by subtracting $\boldsymbol{Q}(\boldsymbol{y})$ from $\boldsymbol{Q}(\boldsymbol{x})$ (which gives a finite integrand, as $\boldsymbol{x} \to \boldsymbol{y}$) and adding

$\boldsymbol{Q}(\boldsymbol{y})$ to the integral (e.g. Pozrikidis 1992, 2001). When $\boldsymbol{y}$ lies on another surface $S_\alpha \neq S_\beta$, the near-singularity subtraction of Loewenberg & Hinch (1996) suggests subtracting $\boldsymbol{Q}(\boldsymbol{x}^*)$ from $\boldsymbol{Q}(\boldsymbol{x})$ in the integrand (3.1), where $\boldsymbol{x}^*$ is the mesh vertex on S_β which is closest to $\boldsymbol{y}$. Although a great improvement, this modification does not completely eliminate the unbounded behaviour of the double-layer integrand when $\boldsymbol{y} \to S_\beta$. This near-singularity subtraction properly adapted to periodic boundary conditions (paper I) allows robust multidrop calculations at low-to-moderate volume fractions and $\lambda = O(1)$, but we have found it insufficient in shear-flow dynamical simulations at high concentrations. In particular, irrespective of the time step used, the velocity iterations were observed to diverge after short strains of $\dot{\gamma}t = 1$–1.5 from the initial well-mixed state of spherical drops at $N \sim 100$ and $c = 0.45$–0.55, even with moderate viscosity contrast $\lambda = 3$ and as many as 1500 triangular elements per drop. Unfortunately, much larger strains are needed for time averaging (§ 5).

In the new near-singularity subtraction developed in the present work, the subtracted quantity $\boldsymbol{Q}^*$ is unrelated to $\boldsymbol{Q}(\boldsymbol{x}^*)$, but is found instead as the solution of a variational problem. Let

$$\triangle S_j = \tfrac{1}{3} \sum \triangle S \tag{3.3}$$

(cf. (3.2) of paper I), where the summation is over all flat mesh triangle areas $\triangle S$ with vertex $\boldsymbol{x}_j$. For fast multidrop simulations, we wish to approximate (3.1), after subtraction, by the simplest trapezoidal rule:

$$\frac{3}{4\pi} \sum_{\boldsymbol{x}_j \in S_\beta} \frac{\left[\boldsymbol{r} \cdot \boldsymbol{W}(\boldsymbol{x}_j)\right] \left[\boldsymbol{r} \cdot (\boldsymbol{Q}(\boldsymbol{x}_j) - \boldsymbol{Q}^*)\right] \boldsymbol{r}}{r^5}, \quad \boldsymbol{r} = \boldsymbol{x}_j - \boldsymbol{y}, \tag{3.4}$$

where

$$\boldsymbol{W}(\boldsymbol{x}_j) = 2\boldsymbol{n}(\boldsymbol{x}_j) \triangle S_j. \tag{3.5}$$

The unknown vector $\boldsymbol{Q}^*$ is required to minimize the Euclidean norm of the discretized double layer (3.4) for a given $\boldsymbol{y}$,

$$\sum_{\boldsymbol{x}_j \in S_\beta} \frac{\left[\boldsymbol{r} \cdot \boldsymbol{W}(\boldsymbol{x}_j)\right]^2 \left[\boldsymbol{r} \cdot (\boldsymbol{Q}(\boldsymbol{x}_j) - \boldsymbol{Q}^*)\right]^2}{r^8} \to \min, \tag{3.6}$$

which gives a linear 3×3 system of equations for $\boldsymbol{Q}^*$:

$$\left[\sum_{\boldsymbol{x}_j \in S_\beta} \frac{\left[\boldsymbol{r} \cdot \boldsymbol{W}(\boldsymbol{x}_j)\right]^2 \boldsymbol{r}\boldsymbol{r}}{r^8} \right] \boldsymbol{Q}^* = \sum_{\boldsymbol{x}_j \in S_\beta} \frac{\left[\boldsymbol{r} \cdot \boldsymbol{W}(\boldsymbol{x}_j)\right]^2 \left[\boldsymbol{r} \cdot \boldsymbol{Q}(\boldsymbol{x}_j)\right] \boldsymbol{r}}{r^8}. \tag{3.7}$$

Using $\boldsymbol{Q}^*$ in place of $\boldsymbol{Q}(\boldsymbol{x}^*)$ in (3.4) greatly improves the spectral properties of the discretized double layer and enables long-time simulations at high concentrations (§ 5), at least for a moderate viscosity ratio. Although $\boldsymbol{Q}^*$ is mostly affected by the nodes $\boldsymbol{x}_j$ close to $\boldsymbol{y}$, it is very important, from our experience, to retain *all* nodes $\boldsymbol{x}_j \in S_\beta$ in the summations (3.7); had we restricted these summations to just a few nodes $\boldsymbol{x}_j$ close to $\boldsymbol{y}$, the velocity iterations would start to diverge after several units of strain at high volume fractions.

We also used a new 'near-singularity' subtraction for the free-space parts:

$$\int_{S_\beta} f(\boldsymbol{x}) \boldsymbol{n}(\boldsymbol{x}) \cdot \mathsf{G}(\boldsymbol{x} - \boldsymbol{y}) \, \mathrm{d}S_x, \quad f(\boldsymbol{x}) = k(\boldsymbol{x}) - \langle k \rangle_\beta \tag{3.8}$$

of the single-layer potential (2.5), where

$$\boldsymbol{G}_o(\boldsymbol{r}) = -\frac{1}{8\pi}\left(\frac{\boldsymbol{I}}{r} + \frac{\boldsymbol{rr}}{r^3}\right) \tag{3.9}$$

is the free-space Green's function and $\boldsymbol{y} \in S_\alpha \neq S_\beta$. Instead of subtracting $f(\boldsymbol{x}^*)$ from $f(\boldsymbol{x})$ (Loewenberg & Hinch 1996), the subtracted quantity f^* in our approach is required to minimize the near-gap contribution to the discretized single-layer potential (3.8) after subtraction:

$$\sum_{\boldsymbol{x}_j \in S_\beta}{}^{*} [f(\boldsymbol{x}_j) - f^*]^2 \left(\triangle S_j\right)^2 [\boldsymbol{n}(\boldsymbol{x}_j) \cdot \boldsymbol{G}_o(\boldsymbol{r})]^2 \to \min. \tag{3.10}$$

In contrast to (3.6)–(3.7), the summation $\sum^*$ includes only the nearest mesh node $\boldsymbol{x}^*$ and all the nodes $\boldsymbol{x}_j \in S_\beta$ adjacent to $\boldsymbol{x}^*$; this modification reflects a slow decay of $\boldsymbol{G}_o(\boldsymbol{x} - \boldsymbol{y})$, compared to $\boldsymbol{\tau}_0(\boldsymbol{x} - \boldsymbol{y})$, as $\boldsymbol{x}$ moves away from the gap. Using (3.9)–(3.10) yields

$$f^* = \frac{\Sigma^* f(\boldsymbol{x}_j)(\triangle S_j/r)^2\{1 + 3[\boldsymbol{r} \cdot \boldsymbol{n}(\boldsymbol{x}_j)/r]^2\}}{\Sigma^*(\triangle S_j/r)^2\{1 + 3[\boldsymbol{r} \cdot \boldsymbol{n}(\boldsymbol{x}_j)/r]^2\}}. \tag{3.11}$$

Although using the new near-singularity subtraction for the single layer is not as crucial as for the double-layer potential, the form (3.11) helps to smooth the subtracted quantity, f^*, compared to $f(\boldsymbol{x}^*)$. For $\boldsymbol{y} \in S_\beta$, regularization of (3.8) is simply made by subtracting $f(\boldsymbol{y})$ from $f(\boldsymbol{x})$ in the integrand of (3.8).

4. Fast calculation of boundary-integral operators

With standard point-to-point summations, the calculation of all the single-layer (2.5) and double-layer (2.7) potentials would require an $O(N^2M^2)$ computational cost (where N is the number of drops in the periodic box and M is the number of collocation points per drop), thus heavily restricting dynamical simulations to small N, even with the fastest calculation of Green's functions $\boldsymbol{G}$ and $\tilde{\boldsymbol{\tau}}$ by suitable interpolations. Instead, a hybrid of boundary-integral and economical multipole techniques is used, following the procedure developed and described in detail in paper I for multidrop sedimentation. This method is briefly outlined below, with an emphasis on the differences between the shear flow and sedimentation problems.

Each drop surface $S_\alpha (\alpha = 1, \ldots, N)$ is represented by an unstructured mesh of flat triangles (figure 2) with vertices $\boldsymbol{x}_j$ (called the collocation nodes). For any smooth integrand $\varphi(\boldsymbol{x})$ on S_α, a simple trapezoidal rule is used, with reassignment of triangle contributions to vertices (Rallison 1981):

$$\int_{S_\alpha} \varphi(\boldsymbol{x})\, \mathrm{d}S \approx \sum_{\boldsymbol{x}_j \in S_\alpha} \varphi(\boldsymbol{x}_j)\triangle S_j, \tag{4.1}$$

with $\triangle S_j$ given by (3.3). The free-space parts $\boldsymbol{G}_0$ and $\boldsymbol{\tau}_0$ (see (3.2) and (3.9)) are singled out from the periodic Stokeslet and stresslet:

$$\boldsymbol{G}(\boldsymbol{r}) = \boldsymbol{G}_0(\boldsymbol{r}) + \boldsymbol{G}_1(\boldsymbol{r}), \quad \tilde{\boldsymbol{\tau}}(\boldsymbol{r}) = \boldsymbol{\tau}_0(\boldsymbol{r}) + \boldsymbol{\tau}_1(\boldsymbol{r}). \tag{4.2}$$

To calculate 'self-interactions', i.e. the contributions of the surface $S_\alpha \ni \boldsymbol{y}$ to the single-layer (2.5) and double-layer (2.7) boundary integrals for collocation nodes $\boldsymbol{y}$, partitions (4.2) are used, and the free-space contributions are calculated by direct summations after the singularity subtractions (relations (3.4)–(3.7) of paper I). The

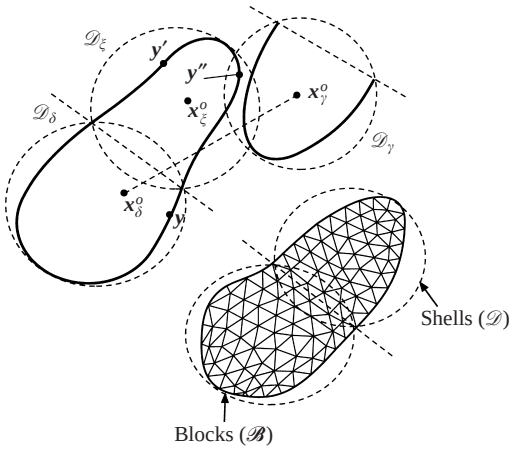

FIGURE 2. On the calculation of near-field interactions. Assuming that shells $\mathscr{D}_\gamma$ and $\mathscr{D}_\delta$ are sufficiently separated, and $\boldsymbol{y}'$ is 'well outside' $\mathscr{D}_\gamma$, the contributions of block $\mathscr{B}_\gamma$ to the boundary integrals for $\boldsymbol{y}$, $\boldsymbol{y}'$ and $\boldsymbol{y}''$ are calculated, respectively, by (i) re-expansion of Lamb's singular series from $\boldsymbol{x}^o_\gamma$ to $\boldsymbol{x}^o_\delta$, (ii) pointwise calculation of Lamb's singular series, and (iii) direct point-to-point summations.

'far-field' contributions to self-interactions (arising from $\mathbf{G}_1$ and $\boldsymbol{\tau}_1$) are calculated by Taylor double series in powers of $(x_j - x^c_\alpha)_k$ and $(y - x^c_\alpha)_\ell$. These expansions are generated to an arbitrary order depending on a 'precision parameter', ε (see below). The number N of drops with centroids $\boldsymbol{x}^c_\alpha \in V$ is assumed to be not too small, so that the minimal spherical shell around S_α centred at $\boldsymbol{x}^c_\alpha$ does not overlap minimal shells around all other periodic images of S_α. This condition guarantees the convergence of the far-field expansions for self-interactions; the larger N, the fewer terms suffice, in general.

A more involved scheme is used to calculate the boundary-integral contributions of surfaces $S_\beta \not\ni \boldsymbol{y}$. Since $\boldsymbol{y}$ may be close to S_β or its periodic images, the near-singularity subtractions are made first, and the integrals (2.5) and (2.7) are then approximated as (cf. (3.8)–(3.9) of paper I)

$$\int_{S_\beta} f(\boldsymbol{x})\mathbf{G}(\boldsymbol{x}-\boldsymbol{y})\cdot\boldsymbol{n}(\boldsymbol{x})\,\mathrm{d}S_{\boldsymbol{x}} \approx \sum_{\boldsymbol{x}_j\in S_\beta} \mathbf{G}(\boldsymbol{x}-\boldsymbol{y})\cdot\boldsymbol{W}(\boldsymbol{x}_j)$$
$$-\sum_{\boldsymbol{k}_{\alpha\beta}} \Theta(\boldsymbol{k}_{\alpha\beta},\boldsymbol{y}) f^* \sum_{\boldsymbol{x}_j\in S_\beta} \mathbf{G}_0(\boldsymbol{x}_j + \boldsymbol{P}(\boldsymbol{k}_{\alpha\beta}) - \boldsymbol{y})\cdot\boldsymbol{n}(\boldsymbol{x}_j)\triangle S_j \qquad (4.3)$$

and

$$2\int_{S_\beta} \boldsymbol{Q}(\boldsymbol{x})\cdot\tilde{\boldsymbol{\tau}}(\boldsymbol{x}-\boldsymbol{y})\cdot\boldsymbol{n}(\boldsymbol{x})\,\mathrm{d}S_{\boldsymbol{x}} \approx \sum_{\boldsymbol{x}_j\in S_\beta} \boldsymbol{Q}(\boldsymbol{x}_j)\cdot\tilde{\boldsymbol{\tau}}(\boldsymbol{x}_j-\boldsymbol{y})\cdot\boldsymbol{W}(\boldsymbol{x}_j)$$
$$-\sum_{\boldsymbol{k}_{\alpha\beta}} \Theta(\boldsymbol{k}_{\alpha\beta},\boldsymbol{y}) \boldsymbol{Q}^* \sum_{\boldsymbol{x}_j\in S_\beta} \boldsymbol{\tau}_0(\boldsymbol{x}_j + \boldsymbol{P}(\boldsymbol{k}_{\alpha\beta}) - \boldsymbol{y})\cdot\boldsymbol{W}(\boldsymbol{x}_j). \qquad (4.4)$$

In (4.3)–(4.4) and in what follows, the weights $\boldsymbol{W}(\boldsymbol{x}_j)$ are

$$\boldsymbol{W}(\boldsymbol{x}_j) = f(\boldsymbol{x}_j)\boldsymbol{n}(\boldsymbol{x}_j)\triangle S_j \qquad (4.5)$$

for the single-layer calculations and are determined by (3.5) for the double-layer calculations. The summations in the second lines of (4.3) and (4.4) are over all integer vectors $\boldsymbol{k}_{\alpha\beta}$ with $||\boldsymbol{x}_\beta^c + \boldsymbol{P}(\boldsymbol{k}_{\alpha\beta}) - \boldsymbol{x}_\alpha^c|| < d_\alpha + d_\beta + h_o$, where d_α and d_β are radii of minimal spherical shells around S_α and S_β centred at $\boldsymbol{x}_\alpha^c$ and $\boldsymbol{x}_\beta^c$, respectively, and h_o is the threshold parameter normally set to $0.3a$. Thus, only periodic images of S_β close to S_α are included in the near-singularity subtractions in the second lines of (4.3) and (4.4). The quantities f^* and $\boldsymbol{Q}^*$ are determined as described in § 3, replacing S_β with its periodic image centred at $\boldsymbol{x}_\beta^c + \boldsymbol{P}(\boldsymbol{k}_{\alpha\beta})$ in all the relations of § 3. The barrier function Θ is

$$\Theta(\boldsymbol{k}_{\alpha\beta}, \boldsymbol{y}) = \max\{1 - ||\boldsymbol{y} - \boldsymbol{x}^* - \boldsymbol{P}(\boldsymbol{k}_{\alpha\beta})||^2/h_o^2,\, 0\}, \tag{4.6}$$

where $\boldsymbol{x}^* \in S_\beta$ is the mesh node which minimizes $||\boldsymbol{x}_j + \boldsymbol{P}(\boldsymbol{k}_{\alpha\beta}) - \boldsymbol{y}||$. According to (4.6), near-singularity subtractions are in effect only when the distance from $\boldsymbol{y}$ to a periodic image of S_β (calculated as the node-to-node minimum) is less than h_o. For $||\boldsymbol{y} - \boldsymbol{x}^* - \boldsymbol{P}(\boldsymbol{k}_{\alpha\beta})|| \ll h_o$, Θ is close to unity, so the terms in the second lines of (4.3) and (4.4) effectively cancel the near-singular behaviour of the terms on the right of the first lines; at the same time, the subtracted terms in (4.3) and (4.4) disappear for fine triangulations. Except for the small-N case, only one image of S_β, namely the one which minimizes the centroid-to-centroid distance from S_α, can contribute to the second sums in (4.3) and (4.4); besides, using the barrier Θ greatly expedites the calculation of these terms in a point-to-point manner. As noted in § 3, it is crucial to use $\boldsymbol{Q}^*$ instead of $\boldsymbol{Q}(\boldsymbol{x}^*)$ in the second line of (4.4) for successful velocity iterations at high concentrations and contrast viscosities in dynamical simulations.

Multipole expansions are used to handle the first sums in (4.3) and (4.4). First, all mesh nodes are organized into compact blocks $\mathscr{B}_1, \ldots, \mathscr{B}_{N_B} (N_B \geqslant N)$. To this end, every drop is cut into

$$\max\left\{\left[\ell_\alpha\left(\frac{2\pi\ell_\alpha}{3V_\alpha}\right)^{1/2} - 1\right], 2\right\} \tag{4.7}$$

pieces by a plane bisecting the line of maximum elongation (figure 2), where ℓ_α is the drop diameter, V_α is the drop volume, and the brackets stand for the greatest integer function. Unlike (3.11) of paper I, the form (4.7) allows a drop to be divided into no more than two blocks, which we have found advantageous in the present calculations (§ 6) with $N \geqslant 50$ and small-to-moderately large deformations. A minimal spherical shell $\mathscr{D}_\gamma$ with a centre $\boldsymbol{x}_\gamma^o$ and radius d_γ^o is constructed around each block $\mathscr{B}_\gamma$ with sufficient accuracy. If a drop S_β is compact and consists of a single block $\mathscr{B}_\gamma$, the block centre $\boldsymbol{x}_\gamma^o$ is not necessarily the surface centroid $\boldsymbol{x}_\beta^c$, and $d_\gamma^o \neq d_\beta$, in general.

As the next step, the free-space single-layer contribution of every block $\mathscr{B}_\gamma (\gamma = 1, \ldots, N_B)$ is expanded in Lamb's singular form:

$$\sum_{\boldsymbol{x}_j \in \mathscr{B}_\gamma} \boldsymbol{G}_0(\boldsymbol{x}_j - \boldsymbol{y}) \cdot \boldsymbol{W}(\boldsymbol{x}_j) = \sum_{v=1}^{\infty}\left[\nabla \times (\boldsymbol{R}_\gamma \chi_{-(v+1)}) + \nabla \Phi_{-(v+1)} - \frac{(v-2)\boldsymbol{R}_\gamma^2 \nabla p_{-(v+1)}}{2v(2v-1)} + \frac{(v+1)p_{-(v+1)}\boldsymbol{R}_\gamma}{v(2v-1)}\right] \tag{4.8}$$

for the weights (4.5). Also, if $\lambda \neq 1$, similar expansions are generated for the free-space

double-layer contributions of every block on each iteration:

$$\sum_{\boldsymbol{x}_j\in\mathscr{B}_\gamma}\boldsymbol{Q}(\boldsymbol{x}_j)\cdot\boldsymbol{\tau}_0(\boldsymbol{x}_j-\boldsymbol{y})\cdot\boldsymbol{W}(\boldsymbol{x}_j)=\sum_{v=1}^{\infty}\left[\nabla\times(\boldsymbol{R}_\gamma\tilde{\chi}_{-(v+1)})+\nabla\tilde{\Phi}_{-(v+1)}\right.$$
$$\left.-\frac{(v-2)\boldsymbol{R}_\gamma^2\nabla\tilde{p}_{-(v+1)}}{2v(2v-1)}+\frac{(v+1)\tilde{p}_{-(v+1)}\boldsymbol{R}_\gamma}{v(2v-1)}\right]+\nabla\tilde{\Phi}_{-1}\qquad(4.9)$$

for the weights (3.5). In (4.8)–(4.9), $\boldsymbol{R}_\gamma=\boldsymbol{y}-\boldsymbol{x}_\gamma^0$, and $p_{-(v+1)}(\boldsymbol{R}_\gamma)$, $\Phi_{-(v+1)}(\boldsymbol{R}_\gamma)$, $\chi_{-(v+1)}(\boldsymbol{R}_\gamma)$, $\tilde{p}_{-(v+1)}(\boldsymbol{R}_\gamma)$, etc. are solid spherical harmonics of order $-(v+1)$. Expansions (4.8)–(4.9) are generated to a sufficient order by an economical rotation-based algorithm (§ 3.2 of paper I) before handling the sums in the first lines of (4.3) and (4.4). Also precalculated is a sufficient number of single-layer

$$\left.\begin{aligned}D_{v,m,k}^{(\gamma)}&=(-1)^v\textstyle\sum_{\boldsymbol{x}_j\in\mathscr{B}_\gamma}Z_{v,m}(\boldsymbol{x}_j-\boldsymbol{x}_\gamma^o)W_k(\boldsymbol{x}_j),\\ E_{v,m,k,\ell}^{(\gamma)}&=(-1)^v\textstyle\sum_{\boldsymbol{x}_j\in\mathscr{B}_\gamma}Z_{v,m}(\boldsymbol{x}_j-\boldsymbol{x}_\gamma^o)W_k(\boldsymbol{x}_j)(x_j-x_j^o)_\ell\end{aligned}\right\}\qquad(4.10)$$

and (if $\lambda\neq1$) double-layer

$$\left.\begin{aligned}\tilde{D}_{v,\mu,k,s}^{(\gamma)}&=(-1)^{v-1}\textstyle\sum_{\boldsymbol{x}_j\in\mathscr{B}_\gamma}W_{(s}(\boldsymbol{x}_j)Q_{k)}(\boldsymbol{x}_j)Z_{v,\mu}(\boldsymbol{x}_j-\boldsymbol{x}_\gamma^o),\\ \tilde{E}_{v,\mu,k,s,\ell}^{(\gamma)}&=(-1)^v\textstyle\sum_{\boldsymbol{x}_j\in\mathscr{B}_\gamma}(x_j-x_\gamma^o)_\ell W_{(s}(\boldsymbol{x}_j)Q_{k)}(\boldsymbol{x}_j)Z_{v,\mu}(\boldsymbol{x}_j-\boldsymbol{x}_\gamma^o)\end{aligned}\right\}\qquad(4.11)$$

'far-field moments' for every block. In (4.10)–(4.11),

$$Z_{v,m}(\boldsymbol{r})=\frac{2\pi^{1/2}r^vY_{v,m}(\boldsymbol{r})}{[(2v+1)(v-m)!(v+m)!]^{1/2}},\qquad(4.12)$$

where $Y_{v,m}(\boldsymbol{r})$ is the standard normalized surface spherical harmonic, and the parentheses round indices denote symmetrization in s and k.

Now, to calculate the sums on the first lines of (4.3) and (4.4) for $\boldsymbol{y}\in\mathscr{B}_\delta\subset S_\alpha$, each block $\mathscr{B}_\gamma$ of the surface $S_\beta\neq S_\alpha$ is temporarily shifted periodically to minimize the centre-to-centre distance $||\boldsymbol{x}_\gamma^o-\boldsymbol{x}_\delta^o||$. The objects associated with the shifted block are still denoted by $\boldsymbol{x}_j$, $\boldsymbol{x}_\gamma^o$, $\mathscr{D}_\gamma$. Also, $\mathsf{G}(\boldsymbol{x}_j-\boldsymbol{y})$ and $\tilde{\boldsymbol{\tau}}(\boldsymbol{x}_j-\boldsymbol{y})$ are split (4.2) into the free-space $\mathsf{G}_0(\boldsymbol{x}_j-\boldsymbol{y})$, $\boldsymbol{\tau}_0(\boldsymbol{x}_j-\boldsymbol{y})$ and far-field $\mathsf{G}_1(\boldsymbol{x}_j-\boldsymbol{y})$, $\boldsymbol{\tau}_1(\boldsymbol{x}_j-\boldsymbol{y})$ parts. If the shells $\mathscr{D}_\delta$ and $\mathscr{D}_\gamma$ do not overlap, the free-space contributions of block $\mathscr{B}_\gamma$ to the sums on the first lines of (4.3) and (4.4) can be evaluated at $\boldsymbol{y}\in\mathscr{B}_\delta$ by first re-expanding (4.8) and (4.9) at $\boldsymbol{x}_\delta^o$ in Lamb's regular form

$$\sum_{n=1}^{\infty}\left[\nabla\times(\boldsymbol{R}_\delta\chi_n)+\nabla\Phi_n+\frac{(n+3)\boldsymbol{R}_\delta^2\nabla p_n}{2(n+1)(2n+3)}-\frac{np_n\boldsymbol{R}_\delta}{(n+1)(2n+3)}\right],\qquad(4.13)$$

where $\boldsymbol{R}_\delta=\boldsymbol{y}-\boldsymbol{x}_\delta^o$ and $p_n(\boldsymbol{R}_\delta)$, $\Phi_n(\boldsymbol{R}_\delta)$ and $\chi_n(\boldsymbol{R}_\delta)$ are solid harmonics of order n. However, only shifted blocks $\mathscr{B}_\gamma$ 'sufficiently separated' from $\mathscr{B}_\delta$ are considered (so that the minimal shells $\mathscr{D}_\gamma$ and $\mathscr{D}_\delta$ around $\mathscr{B}_\delta$ and $\mathscr{B}_\gamma$ have enough clearance for sufficient convergence of (4.13)), and contributions from all such blocks $\mathscr{B}_\gamma$ to (4.13) are accumulated, using a fast, rotation-based re-expansion algorithm (§ 3.3 of paper I). The cumulative series (4.13) are calculated for all $\boldsymbol{y}\in\mathscr{B}_\delta$ in a pointwise manner.

If a shifted block $\mathscr{B}_\gamma$ is not 'sufficiently separated' from $\mathscr{B}_\delta$, but node $\boldsymbol{y}\in\mathscr{B}_\delta$ is 'well outside' the shell $\mathscr{D}_\gamma$, Lamb's singular series (4.8)–(4.9) are used directly to calculate

the left-hand sides of (4.8)–(4.9). Only in rare cases, when $\boldsymbol{y}$ is inside $\mathscr{D}_\gamma$, or is outside but too close to $\mathscr{D}_\gamma$, should we use standard point-to-point summations (4.8)–(4.9).

The far-field contributions of the shifted block $\mathscr{B}_\gamma$, i.e. the left-hand sides of (4.8) and (4.9) with $\mathsf{G}_1(\boldsymbol{x}_j-\boldsymbol{y})$ and $\boldsymbol{\tau}_1(\boldsymbol{x}_j-\boldsymbol{y})$ instead of $\mathsf{G}_0(\boldsymbol{x}_j-\boldsymbol{y})$ and $\boldsymbol{\tau}_0(\boldsymbol{x}_j-\boldsymbol{y})$, respectively, can be evaluated at $\boldsymbol{y}\in\mathscr{B}_\delta$ by a special form of Taylor double series in powers of $\boldsymbol{x}_j-\boldsymbol{x}_\gamma^o$ and $\boldsymbol{y}-\boldsymbol{x}_\delta^o$ for Stokes flows (§ 3.4 of paper I):

$$\sum_{\boldsymbol{x}_j\in\mathscr{B}_\gamma} W_k(\boldsymbol{x}_j)(G_1)_{k\ell}(\boldsymbol{x}_j-\boldsymbol{y})$$
$$=\sum_{n=0}^{\infty}\sum_{m=-n}^{n} Z_{n,m}(\boldsymbol{R}_\delta)\left\{\sum_{\nu=0}^{\infty}\sum_{\mu=-\nu}^{\nu}\left[D^{(\gamma)}_{\nu,\mu,k}\partial_{n+\nu,m+\mu}g_{k\ell}(\boldsymbol{R}_{\gamma\delta})\right.\right.$$
$$\left.\left.-\tfrac{1}{2}E^{(\gamma)}_{\nu,\mu,k,\ell}\partial_{n+\nu,m+\mu}q_1^{(k)}(\boldsymbol{R}_{\gamma\delta})+\tfrac{1}{2}(R_{\gamma\delta})_\ell D^{(\gamma)}_{\nu,\mu,k}\partial_{n+\nu,m+\mu}q_1^{(k)}(\boldsymbol{R}_{\gamma\delta})\right]\right\}$$
$$+\tfrac{1}{2}(R_\delta)_\ell\sum_{n=0}^{\infty}\sum_{m=-n}^{n} Z_{n,m}(\boldsymbol{R}_\delta)\sum_{\nu=0}^{\infty}\sum_{\mu=-\nu}^{\nu} D^{(\gamma)}_{\nu,\mu,k}\partial_{n+\nu,m+\mu}q_1^{(k)}(\boldsymbol{R}_{\gamma\delta}), \tag{4.14}$$

$$\sum_{\boldsymbol{x}_j\in\mathscr{B}_\gamma} Q_s(\boldsymbol{x}_j)(\tau_1)_{ks\ell}(\boldsymbol{x}_j-\boldsymbol{y})W_k(\boldsymbol{x}_j)$$
$$=\sum_{n=0}^{\infty}\sum_{m=-n}^{n} Z_{n,m}(\boldsymbol{R}_\delta)\left\{\sum_{\nu=0}^{\infty}\sum_{\mu=-\nu}^{\nu}\left[\tilde{D}^{(\gamma)}_{\nu,\mu,k,s}\partial_{n+\nu,m+\mu}t_{ks\ell}(\boldsymbol{R}_{\gamma\delta})\right.\right.$$
$$\left.\left.+\tfrac{1}{2}\tilde{E}^{(\gamma)}_{\nu,\mu,k,s,\ell}\partial_{n+\nu,m+\mu}\tilde{q}_1^{(ks)}(\boldsymbol{R}_{\gamma\delta})+\tfrac{1}{2}(R_{\gamma\delta})_\ell\tilde{D}^{(\gamma)}_{\nu,\mu,k,s}\partial_{n+\nu,m+\mu}\tilde{q}_1^{(ks)}(\boldsymbol{R}_{\gamma\delta})\right]\right\}$$
$$+\tfrac{1}{2}(R_\delta)_\ell\sum_{n=0}^{\infty}\sum_{m=-n}^{n} Z_{n,m}(\boldsymbol{R}_\delta)\sum_{\nu=0}^{\infty}\sum_{\mu=-\nu}^{\nu}\tilde{D}^{(\gamma)}_{\nu,\mu,k,s}\partial_{n+\nu,m+\mu}\tilde{q}_1^{(ks)}(\boldsymbol{R}_{\gamma\delta}). \tag{4.15}$$

Here, $\boldsymbol{R}_{\gamma\delta}=\boldsymbol{x}_\delta^o-\boldsymbol{x}_\gamma^o$ is the minimal block-to-block vector (for the shear flow problem, $\boldsymbol{R}_{\gamma\delta}$ does not necessarily belong to the cell $V=\{\xi^i\boldsymbol{e}_i,\ |\xi^i|\leqslant 1/2\}$), $\partial_{\nu,\mu}=(D_1-\mathrm{i}D_2)^\mu D_3^{\nu-|\mu|}$, where D_i is the partial derivative with respect to ith Cartesian coordinate and $(D_1-\mathrm{i}D_2)^\mu=(-1)^\mu(D_1+\mathrm{i}D_2)^{-\mu}$ for $\mu<0$,

$$g_{k\ell}(\boldsymbol{r})=(G_1)_{k\ell}-\tfrac{1}{2}q_1^{(k)}(\boldsymbol{r})r_\ell, \tag{4.16}$$

where $q_1^{(k)}(\boldsymbol{r})$ is the pressure associated with the Stokes velocity $((G_1)_{k1},(G_1)_{k2},(G_1)_{k3})$,

$$t_{ks\ell}(\boldsymbol{r})=(\tau_1)_{ks\ell}(\boldsymbol{r})-\tfrac{1}{2}\tilde{q}_1^{(ks)}(\boldsymbol{r})r_\ell, \tag{4.17}$$

where $\tilde{q}_1^{(ks)}(\boldsymbol{r})$ is the pressure associated with the velocity $((\tau_1)_{ks1},(\tau_1)_{ks2},(\tau_1)_{ks3})$, and $D^{(\gamma)}_{\nu,\mu,k}$, $E^{(\gamma)}_{\nu,\mu,k,\ell}$, $\tilde{D}^{(\gamma)}_{\nu,\mu,k,s}$, and $\tilde{E}^{(\gamma)}_{\nu,\mu,k,s,\ell}$ are the far-field moments (4.10)–(4.11). As shown in § 3.4 of paper I, the derivatives in (4.15) can be expressed in terms of $\partial_{n,m}\boldsymbol{g}$ and $\partial_{n,m}\boldsymbol{q}_1$. The number N of drops in the cell is assumed to be not too small, so that the shell $\mathscr{D}_\delta$ does not overlap any periodic images of $\mathscr{D}_\gamma$, except possibly $\mathscr{D}_\gamma$ itself, which guarantees the convergence of the far-field expansions (4.14)–(4.15); in general, the larger N, the fewer terms suffice. Calculation of the far-field parts of self interactions (see above) is a particular case of (4.14)–(4.15), when the summations in (4.10)–(4.11)

and (4.14)–(4.15) are over the entire drop surface S_α, $\delta = \gamma = \alpha$, $\boldsymbol{R}_{\gamma\delta} = 0$, and $\boldsymbol{x}_\delta^o = \boldsymbol{x}_\gamma^o$ is set to $\boldsymbol{x}_\alpha^c$.

For the multidrop sedimentation problem, the periodic cell V is a stationary cube, and all the necessary derivatives $\partial_{n,m} g_{k\ell}$ and $\partial_{n,m} q_1^{(k)}$ for (4.14)–(4.15) could be tabulated prior to dynamical simulations. A new difficulty in the present case of shear flow is the time dependence of the periodic cell V, making the task of precalculating the derivatives $\partial_{n,m} g_{k\ell}$ and $\partial_{n,m} q_1^{(k)}$ prohibitive in terms of memory and disk space requirements (since, at high concentrations and $N = O(100)$, the derivatives of order $n = O(10)$ are typically needed). In Appendix B, a fast algorithm is offered for dynamical calculation of $\partial_{n,m} g_{k,\ell}$ and $\partial_{n,m} q_1^{(k)}$, to avoid this difficulty. In the present implementation, the far-field, $O(N^2)$ part is fast compared to the rest of the code, and the whole algorithm scales practically linearly in N, as long as $N < 1000$ (assuming that $N_\triangle = O(10^3)$ boundary elements per drop are used; see Appendix B for more detail).

An essential feature of the present algorithm, as well as that of paper I, is the 'economical truncation' of multipole expansions/re-expansions, depending on a single precision parameter ε for optimized performance. In particular, we take into account that the rate of convergence of the re-expansion from (4.8) or (4.9) to (4.13) strongly depends on the clearance between the shells $\mathscr{D}_\delta$ and $\mathscr{D}_\gamma$; likewise, the number of terms on the right-hand sides of (4.8) or (4.9) to be retained for pointwise calculations is a strong function of $||\boldsymbol{y} - \boldsymbol{x}_\gamma^o||/d_\gamma^o$. To construct the economical truncation bounds, the algorithm of § 3.5 of paper I starts from the estimation of the coefficients a_k in the expansion

$$\sum_{x_\gamma \in \mathscr{B}_\gamma} \mathbf{G}_0(\boldsymbol{x}_j - \boldsymbol{y}) \cdot \boldsymbol{W}(\boldsymbol{x}_j) = \sum_{k=0}^{\infty} a_k \left(\frac{d_\gamma^o}{R_\gamma} \right)^{k+1}, \quad R_\gamma = |\boldsymbol{y} - \boldsymbol{x}_\gamma^o| > d_\gamma^o \tag{4.18}$$

for a block $\mathscr{B}_\gamma$, where, for small k, a model behaviour $|a_k| = C_\gamma/(k+1)^3$ with $C_\gamma = \text{const}$ is assumed. Unlike in the sedimentation problem, however, it would be unreliable for force-free drops to estimate C_γ from a_o, since the sum of the single-layer weights (3.6) over all $\boldsymbol{x}_\gamma \in \mathscr{B}_\gamma$ is zero (to within triangulation errors), if the block $\mathscr{B}_\gamma$ constitutes a whole drop. Instead, an explicit form (3.9) and Taylor expansion yield, for $R_\gamma \gg d_\gamma^o$,

$$\begin{aligned} -8\pi \mathbf{G}_0(\boldsymbol{x}_j - \boldsymbol{y}) \cdot \boldsymbol{W}(\boldsymbol{x}_j) \sim \frac{\boldsymbol{W}}{R_\gamma} + \frac{(\boldsymbol{W} \cdot \boldsymbol{R}_\gamma)\boldsymbol{R}_\gamma}{R_\gamma^3} + \frac{(\boldsymbol{R}_\gamma \cdot \Delta\boldsymbol{x})\boldsymbol{W}}{R_\gamma^3} \\ - \frac{(\boldsymbol{W} \cdot \boldsymbol{R}_\gamma)\Delta\boldsymbol{x}}{R_\gamma^3} - \frac{(\boldsymbol{W} \cdot \Delta\boldsymbol{x})\boldsymbol{R}_\gamma}{R_\gamma^3} + \frac{3(\boldsymbol{R}_\gamma \cdot \Delta\boldsymbol{x})(\boldsymbol{W} \cdot \boldsymbol{R})\boldsymbol{R}}{R_\gamma^5}, \end{aligned} \tag{4.19}$$

where, for brevity, $\boldsymbol{W} = \boldsymbol{W}(\boldsymbol{x}_j)$ and $\Delta\boldsymbol{x} = \boldsymbol{x}_j - \boldsymbol{x}_\gamma^o$. Substituting (4.19) into the left-hand side of (4.18), an upper bound on the $O(R_\gamma^{-2})$ term can be found through invariants of the tensor

$$\boldsymbol{T}_\gamma = \sum_{\boldsymbol{x}_\gamma \in \mathscr{B}_\gamma} (\boldsymbol{x}_j - \boldsymbol{x}_\gamma^o)\boldsymbol{W}(\boldsymbol{x}_j). \tag{4.20}$$

Comparing the result with the right-hand side of (4.18) at $k = 1$ suggests the estimate

$$C_\gamma = \frac{1}{\pi (d_\gamma^o)^2} [||\boldsymbol{T}_\gamma - \boldsymbol{T}_\gamma^*|| + |\mathrm{tr}\boldsymbol{T}_\gamma| + 3||\boldsymbol{T}_\gamma||], \tag{4.21}$$

where an asterisk stands for the transpose, and Euclidean norms are used for the matrices. Relation (4.21) replaces (3.85) of paper I for the present problem, but

otherwise the construction of near-field truncation bounds $v_{nf}(\delta,\gamma)$, $n_{nf}(\delta,\gamma)$, $\tilde{v}_{nf}(\delta,\gamma)$, and $\tilde{n}_{nf}(\delta,\gamma)$ for the re-expansions from (4.8)–(4.9) to (4.13), and the bounds v^*_{nf}, and $\tilde{v}^*_{nf}$ for pointwise calculations of the right-hand side of (4.8)–(4.9) repeats (3.82)–(3.92) of paper I without changes. Using (3.94) of that paper, $\boldsymbol{R}_{\delta\gamma}+\boldsymbol{m}$ (where $\boldsymbol{R}_{\delta\gamma}=\boldsymbol{x}^o_\gamma-\boldsymbol{x}^o_\delta$ is the minimal block-to-block vector after the shift of $\mathscr{B}_\gamma$) must be replaced by $\boldsymbol{R}_{\delta\gamma}+\boldsymbol{P}(\boldsymbol{m})$, in accordance with the geometry of the skewed lattice (2.1); this is the only change needed to calculate the far-field truncation bounds v_{ff}, n_{ff}, and v^*_{ff} for (4.14), and $\tilde{v}_{ff}$, $\tilde{n}_{ff}$, and $\tilde{v}^*_{ff}$ for (4.15) in the present problem. Parameters $e_{nf}=1$, $e_{ff}=10$, $\tilde{e}_{nf}=0.2$, and $\tilde{e}_{ff}=10$ (cf. paper I) balancing the near/far-field truncation errors for the inhomogeneous $\boldsymbol{F}(\boldsymbol{y})$ and double-layer terms in (2.7) are selected. With fixed e_{nf}, e_{ff}, $\tilde{e}_{nf}$, and $\tilde{e}_{ff}$, our truncation scheme depends on a single precision parameter ε, and all multipoles are eventually included, as $\varepsilon\to 0$. However, for optimized performance, a threshold order $k_o\sim 20$ is set to limit the use of multipoles in near-field expansions/re-expansions; if a truncation bound exceeds k_o, pointwise boundary-integral operations are invoked instead as in paper I.

Due to a somewhat empirical construction of economical truncation bounds, the 'precision' ε is not a deviation from the non-multipole solution in a rigorous sense, but it does correlate with this deviation (§ 5). The condition $\varepsilon \ll a$ is roughly required for the truncation errors to be small compared to the microstructural velocity $O(a)$ (in the sedimentation problem, we had $\varepsilon \ll a^2$). Unless otherwise stated, $\varepsilon = 10^{-3}a$ was used in the present calculations; the effect of ε on dynamical simulations is discussed in § 5. Recall that $a = a_o/L$ is the non-dimensional radius of an undeformed drop.

5. Numerical results

5.1. *Tests for dilute and periodic systems*

Due to the large size of our hybrid multipole–boundary-integral code, it was crucial to test it against known solutions in special cases. In table 1, our steady-state particle stresses $\Sigma^P_{12}=Ca(\mu^*-1)/c$, $N^P_1=Ca\,N_1/c$ and $N^P_2=Ca\,N_2/c$ for dilute emulsions are compared with those read from figure 9(a,b) of Kennedy *et al.* (1994); for every Ca and λ, a column $(\Sigma^P_{12},\ N^P_1,\ N^P_2)$ is given. Our results were obtained for random emulsions with $N=8$ drops in a periodic cell and $N_\triangle=1280$ triangular elements per drop at drop volume fraction $c=10^{-4}$, while the calculations of Kennedy *et al.* (1994) in table 1 are for one drop with 384 quadratic boundary elements in a shear flow. Considering some uncertainty of reading from the graphs of Kennedy *et al.* (1994), especially for small N^P_2, the agreement between the two methods in table 1 is generally very good.

Sangani & Lu (1987) calculated the instantaneous shear viscosity $\mu^*=1+\beta$ of concentrated emulsions of spherical drops in a simple cubic array for different λ and $\chi=(c/c_{\max})^{1/3}$, with $c_{\max}=\pi/6$. It is a non-trivial matter to reproduce the $Ca=0$ limit in boundary-integral calculations for deformable drops, and dynamical simulations are required, since small dynamically formed $O(Ca)$ deviations from the spherical shape have an $O(1)$ effect on the stress tensor (see (2.8)). For the comparison with the solution of Sangani & Lu (1987), we considered small but finite Ca, and arranged $N=27$ initially spherical drops with $\lambda=5$ in a cubic cell to form a simple cubic array with $\chi=0.95$ at $t=0$ (figure 3). With these special initial conditions, all drops deform and move identically at $t>0$, each drop stays in its own subcell of periodicity (figure 3), and the problem is equivalent to the transient behaviour of an ordered emulsion of deformable drops (one drop per cell), the lattice being

		Present code ($N_\triangle = 1280$)		Kennedy *et al.* (1994)	
		$\lambda = 1$	$\lambda = 6.4$	$\lambda = 1$	$\lambda = 6.4$
(*a*)	Σ_{12}^P	0.318	0.392	0.315	0.390
	N_1^P	0.296	0.135	0.285	0.120
	N_2^P	−0.079	−0.028	−0.080	–
(*b*)	Σ_{12}^P	0.421	0.558	0.420	0.565
	N_1^P	0.645	0.186	0.625	0.180
	N_2^P	−0.155	−0.037	−0.160	−0.040
(*c*)	Σ_{12}^P	–	0.884	–	0.880
	N_1^P	–	0.241	–	0.250
	N_2^P	–	−0.046	–	−0.055

TABLE 1. Particle stresses Σ_{12}^P, N_1^P, N_2^P for dilute emulsions of deformable drops: (*a*) $Ca = 0.2$, (*b*) $Ca = 0.3$, (*c*) $Ca = 0.5$.

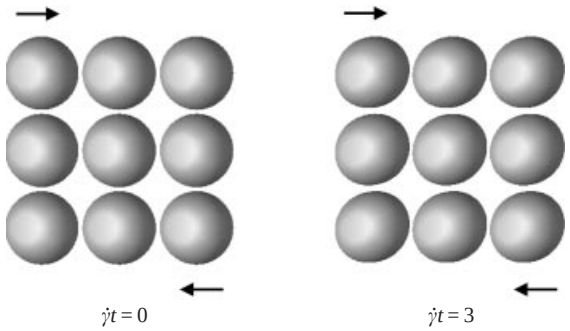

FIGURE 3. Simulation of the shear flow with $N = 27$ drops in the periodic cell at $(c/c_{\max}) = 0.95$, $\lambda = 5$, $Ca = 0.025$ and $N_\triangle = 1280$ starting from special initial conditions. At $t = 0$, drops are spherical and are chosen to form a simple cubic array. At strain $\dot{\gamma}t = 3$, drops become slightly deformed, but remain perfectly layered. Only nine out of 27 drops in the plane of shear are shown in each case.

skewed by the shear flow; this problem was formulated by Pozrikidis (1993). In figure 4(*a*), our shear viscosity μ^* is plotted vs. strain $\dot{\gamma}t$ for $Ca = 0.05$, 0.025, and 0.0125, and $N_\triangle = 1280$; using $N_\triangle = 720$ instead of 1280 at $Ca = 0.025$ did not show any appreciable changes. For $Ca = 0.05$, strains $\dot{\gamma}t = 2$–3 are needed to reach the periodic regime, while for $Ca = 0.0125$ strains of $\dot{\gamma}t = 1$ suffice. At integer strains $\dot{\gamma}t = k$ ($k \to \infty$), when the periodic lattice is a simple cubic array, our viscosities are 2.46, 2.395, and 2.328 for $Ca = 0.05$, 0.025, and 0.0125, respectively. As $Ca \to 0$, these results closely approach the viscosity $\mu^* = 2.290$ of simple cubic arrays of spherical drops at $\lambda = 5$ and $\chi = 0.95$ from table 3 of Sangani & Lu (1987). A similar comparison was made at $\chi = 0.9$ (figure 4*b*), when the periodic regimes are reached even more rapidly; again, our viscosities of 2.056, 2.027, and 1.996 for $Ca = 0.05$, 0.025, and 0.0125, respectively, at large integer strains $\dot{\gamma}t = k \to \infty$ tend to the result $\mu^* = 1.981$ of Sangani & Lu (1987), as $Ca \to 0$. Interestingly, the limiting viscosity for spherical drops is approached from above (unlike for random emulsions, see § 5.2).

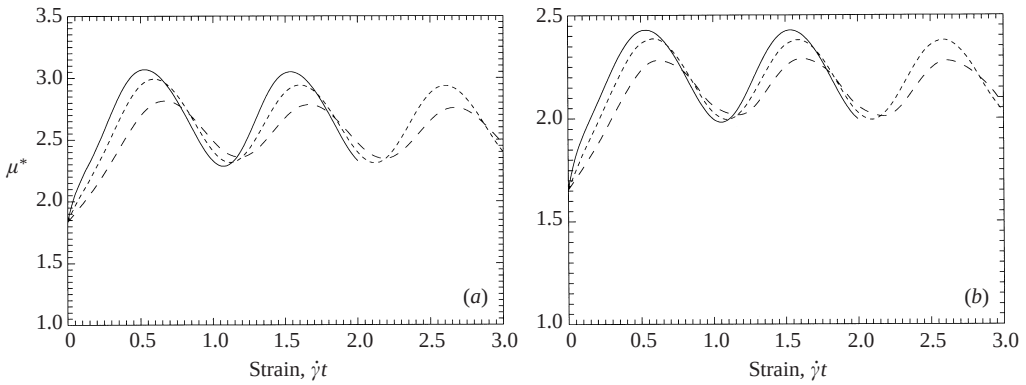

FIGURE 4. (*a*) The dimensionless viscosity μ^* vs. strain for the simulation shown in figure 3 (short-dashed line) and two similar simulations using $Ca = 0.05$ (long-dashed line) and $Ca = 0.0125$ (solid line); (*b*) the same as (*a*) but at $c/c_{\max} = 0.9$.

In addition to the results of Sangani & Lu (1978), Pozrikidis (1993) derived an asymptotic relation for the time-averaged viscosity of dilute sheared periodic emulsions of spherical drops which form initially a simple cubic array:

$$\mu^* = 1 + 2.5\gamma c(1 + 0.1368\gamma c - 1.403\delta c^{2/3}), \quad c \to 0, \tag{5.1}$$

with $\gamma = (\lambda + 2/5)/(\lambda + 1)$ and $\delta = \lambda/(\lambda + 1)$. Relation (5.1) is believed to be accurate in a wide range of χ (when $\lambda = O(1)$), except for the vicinity $\chi \approx 1$ of close packing (Pozrikidis 1993). Our simulation at $\chi = 0.7$, $\lambda = 1$, $Ca = 0.0125$, $N = 27$, and $N_\triangle = 1280$, similar to those in figures 4(*a*, *b*) yields the time-averaged viscosity (after the periodic regime is established) of $\mu^* = 1.326$, which is indeed in an excellent agreement with $\mu^* = 1.322$ from (5.1). Note that these tests at $N = 27$ validate both the near-field and the far-field interaction parts of our code, as well as the deformation part. (On the other hand, these tests show the importance of choosing *random* initial configurations in dynamical simulations for real emulsions; otherwise, special initial conditions may have an extremely long memory.) Pozrikidis (1993) also considered shear flow of periodic emulsions ($N = 1$) at finite Ca, but, due to accuracy limitations mentioned in his paper, we have not attempted a comparison with our code in this case. Two more comprehensive tests for our code are discussed below.

5.2. *Random concentrated emulsions*

In our dynamical simulations for random concentrated systems, an initial state at $t = 0$ was typically a random, 'well-mixed' arrangement of spherical drops with equal probability of all non-overlapping configurations prepared by the standard Monte-Carlo method (e.g. MacKeown 1997). With one exception (see below), at least several million Monte-Carlo steps were always used, so that our initial packings with $N = 100$–200 did not suffer from metastability at the highest concentration $c = 0.55$ considered, but were always in 'thermodynamical equilibrium'. At $c = 0.55$, such states are known to have partial order. In contrast to sedimenting emulsions of deformable drops, which always cluster (paper I), an emulsion of drops suspended in shear flow is always expected to reach a statistical steady state for subcritical breakup conditions (Loewenberg & Hinch 1996). In a few cases, we selected as the initial condition a statistical steady-state configuration reached for a different Ca or λ, although this strategy showed only minor advantages in the present calculations.

Figure 5 presents a typical snapshot of one of our simulations with $\lambda = 1$, $c = 0.5$,

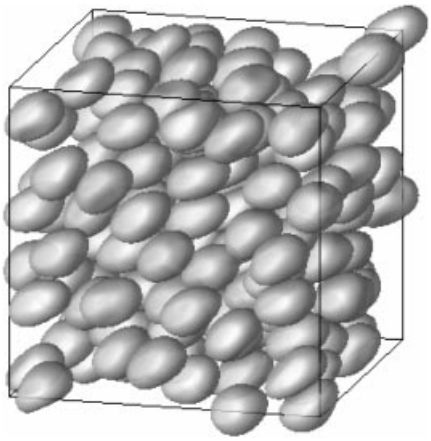

FIGURE 5. A snapshot of the dynamical simulation for $c = 0.5$, $\lambda = 1$, $Ca = 0.1$, $N = 200$ and $N_\triangle = 1280$ at the steady-state strain of $\dot{\gamma}t = 4.45$. The centres of 200 independent drops have been mapped into $(0,1)^3$, an initial periodic cell.

$Ca = 0.1$, $N = 200$ and $N_\triangle = 1280$ at the steady-state strain of $\dot{\gamma}t = 4.45$; only 200 drops with centres in $(0,1) \times (0,1) \times (0,1)$, an initial periodic cell, are shown. The whole simulation was done from $t = 0$ (when drops are spherical) to $\dot{\gamma}t \approx 28$ by the second-order Runge–Kutta integration scheme with a constant strain step $\dot{\gamma}\Delta t = 0.01$. For the typical snapshot in figure 5, one half of the second-order step took 178 s on a DEC 600au workstation. Of this, 153 s are spent on boundary integrals (2.5) (with all overheads for far- and near-field moments, drop partitioning into blocks, truncation bounds, etc. (§ 4) and dynamical pretabulation of the Green function derivatives (Appendix B) with $N_T = 6$), plus 12 s for normal and curvature calculations by BPS (§ 2) and 13 s for passive mesh stabilizations (Appendix A). As an essential validation of our hybrid boundary-integral–multipole code for arbitrary configurations and shapes, we compared, for the snapshot in figure 5, our boundary integrals (2.5) for $\boldsymbol{F}(\boldsymbol{x}_i)$ with exact values $\boldsymbol{F}_{ex}(\boldsymbol{x}_i)$ (for a given triangulation) obtained by standard point-to-point summations in the first line of (4.3) and similar 'self-integrals' (see (3.4*a*) of paper I), i.e. without drop partitioning into blocks and multipoles. In the point-to-point scheme, the free-space part $\boldsymbol{G}_0$ of the Green function $\boldsymbol{G}(\boldsymbol{x}_j - \boldsymbol{y})$ was subtracted out (as in Loewenberg & Hinch 1996), and the remainder $\boldsymbol{G}_1(\boldsymbol{\xi})$ was calculated in the periodic cell $V = \{\xi^i \boldsymbol{e}_i,\ |\xi^i| \leqslant 1/2\}$ as the quadratic Taylor approximation at the nearest node of a $91 \times 91 \times 91$ mesh in V through tabulated derivatives of $\boldsymbol{G}_1$ to the second order in V and symmetry properties. Such a fine mesh and quadratic interpolation were chosen only for the most accurate comparison, to exclude any appreciable errors in $\boldsymbol{G}(\boldsymbol{x}_j - \boldsymbol{y})$. Of interest is the excess velocity field $\Delta\boldsymbol{u}(\boldsymbol{y}) = \boldsymbol{F}(\boldsymbol{y}) - \boldsymbol{u}_\infty(\boldsymbol{y})$ (for $\lambda = 1$) which determines the microstructural dynamics, rather than $\boldsymbol{F}(\boldsymbol{y})$, and we used three criteria to quantify the difference between $\Delta\boldsymbol{u}(\boldsymbol{y})$ and $\Delta\boldsymbol{u}_{ex}(\boldsymbol{y}) = \boldsymbol{F}_{ex}(\boldsymbol{y}) - \boldsymbol{u}_\infty(\boldsymbol{y})$:

$$\delta_1(\Delta\boldsymbol{u},\, \Delta\boldsymbol{u}_{ex}) = \frac{1}{\langle \Delta\boldsymbol{u}_{ex}^2 \rangle^{1/2}} \max_{\alpha,\, \boldsymbol{x}_i \in S_\alpha} ||\Delta\boldsymbol{u}(\boldsymbol{x}_i) - \Delta\boldsymbol{u}_{ex}(\boldsymbol{x}_i)||, \tag{5.2a}$$

$$\delta_2(\Delta\boldsymbol{u},\, \Delta\boldsymbol{u}_{ex}) = \frac{1}{N} \sum_{\alpha=1}^{N} \left\{ \frac{1}{\langle \Delta\boldsymbol{u}_{ex}^2 \rangle_\alpha} \max_{\boldsymbol{x}_i \in S_\alpha} [\Delta\boldsymbol{u}(\boldsymbol{x}_i) - \Delta\boldsymbol{u}_{ex}(\boldsymbol{x}_i)]^2 \right\}^{1/2}, \tag{5.2b}$$

$$\delta_3(\Delta\boldsymbol{u},\ \Delta\boldsymbol{u}_{ex}) = \left[\langle(\Delta\boldsymbol{u}-\Delta\boldsymbol{u}_{ex})^2\rangle \Big/ \langle(\Delta\boldsymbol{u}_{ex})^2\rangle\right]^{1/2}. \tag{5.2c}$$

Here $\langle\cdots\rangle_\alpha$ and $\langle\cdots\rangle$ denote averaging over S_α and all surfaces, respectively. In table 2, $\delta_i(\Delta\boldsymbol{u},\ \Delta\boldsymbol{u}_{ex})$ and the CPU times (in seconds) for the calculation of all the boundary integrals (2.5) by the present method on a DEC 600au are given vs. the precision parameter ε (§4), for drop partitioning into blocks (i) enabled (with a total of 241 blocks) and (ii) disabled. Using drop partitioning in this case helps to reduce the errors δ_i, especially the maximum deviation from $\Delta\boldsymbol{u}_{ex}$, with negligible changes in the CPU times. All errors δ_i strongly correlate with the intuitive precision parameter ε and tend to zero, as $\varepsilon \to 0$, which proves the convergence of our code to the standard point-to-point scheme. The comparison of small $\Delta\boldsymbol{u} \sim a$ and $\Delta\boldsymbol{u}_{ex}$ is a more stringent test than that of $\boldsymbol{F}$ and $\boldsymbol{F}_{ex}$. At $\varepsilon = 10^{-3}a$ and drop partitioning enabled (as in dynamical simulations for figure 5), it takes our code only 153 s to calculate all the boundary integrals (2.5). In comparison, direct point-to-point summations were impractically slow (about 203 min of CPU time) prohibiting dynamical simulations of such large systems by the standard method. At high drop volume fractions $c \geqslant 0.5$, the performance of our hybrid code slightly degrades in computational efficiency (roughly 1.5–1.6 times for $N \sim 10^2$ and $N_\triangle \sim 10^3$) compared to the case of moderate concentrations $c \sim 0.25$ (paper I); primarily, this degradation is due to the increased weight of costly direct summations for densely located drops. Nevertheless, the observed almost 80-fold gain over the standard method is significant. Precisions $\varepsilon \sim 10^{-3}a$ have a surprisingly small effect on the results of dynamical simulations (see below) and could probably be relaxed, with modest additional savings in the CPU time (table 2).

Although small systems ($N \sim 10$) can be simulated by the much simpler direct boundary-integral method, we have found that it is quite important to use much larger systems ($N \geqslant 0(10^2)$) in emulsion rheology simulations at high drop volume fractions for two reasons. First, the statistical fluctuations for small systems are much larger, necessitating larger strain intervals for averaging the results. In figure 6(*a–c*), the trajectories of the shear viscosity μ^* and normal stress differences N_1 and N_2 vs. strain at $c = 0.5$, $\lambda = 1$, $Ca = 0.05$ and $N_\triangle = 1280$ are shown for two simulations using $N = 10$ (dashed lines) and $N = 100$ (solid lines). For $N = 10$, our hybrid scheme of §4 would not give any particular advantages (and, moreover, would be difficult to use without modifications at high c because of slow convergence/divergence of far-field expansions in this case), so we used a direct boundary-integral method. With $N = 10$, statistical fluctuations are particularly large for N_1 (figure 6*b*) and require strains of $\dot\gamma t \sim 10^2$ for averaging (after an unsteady part of the trajectory has been cut off); in contrast, for $N = 100$, strains of 30–40 suffice to obtain average steady-state values for $\langle\mu^*\rangle$, $\langle N_1\rangle$, $\langle N_2\rangle$ with absolute errors of ± 0.02, ± 0.04, and ± 0.03, respectively (here and henceforth statistical error estimates correspond to 67% confidence intervals). For $N = 100$, each half of the second-order Runge–Kutta time step by our hybrid method takes about 77 s on a DEC 600au, which is only two times greater than that for $N = 10$ by the standard method. For this reason, considering small systems ($N \sim 10$) does not offer computational advantages at high concentrations. When $Ca \to 0$, relatively large statistical fluctuations are observed even in the calculations with 200 drops (figure 7*a–c*).

Secondly, and most importantly, when statistical errors for $N \sim 10$ are eliminated by adequate averaging, the systematic errors can still be quite large, especially for the normal stress differences. Figure 8(*a–c*) presents comparisons of $\langle\mu^*\rangle$, $\langle N_1\rangle$ and $\langle N_2\rangle$ at $c = 0.5$ and $\lambda = 1$ for $N = 10$, 50, 100, and 200. To obtain the results in figure 8(*a–*

	With drop partitioning				Without drop partitioning			
ε	δ_1	δ_2	δ_3	CPU time (s)	δ_1	δ_2	δ_3	CPU time (s)
$10^{-2}a$	5.3×10^{-2}	2.3×10^{-2}	7.4×10^{-3}	121	1.1×10^{-1}	2.8×10^{-2}	9.0×10^{-3}	119
$3 \times 10^{-3}a$	2.8×10^{-2}	8.6×10^{-3}	2.7×10^{-3}	136	4.2×10^{-2}	1.0×10^{-2}	3.4×10^{-3}	134
$10^{-3}a$	7.9×10^{-3}	3.3×10^{-3}	1.1×10^{-3}	153	1.7×10^{-2}	3.9×10^{-3}	1.3×10^{-3}	150
$3 \times 10^{-4}a$	3.8×10^{-3}	1.1×10^{-3}	3.7×10^{-4}	176	6.7×10^{-3}	1.4×10^{-3}	4.7×10^{-4}	172
$10^{-4}a$	1.3×10^{-3}	4.2×10^{-4}	1.4×10^{-4}	203	2.4×10^{-3}	4.9×10^{-4}	1.7×10^{-4}	198
$10^{-5}a$	1.9×10^{-4}	6.0×10^{-5}	2.4×10^{-5}	266	2.9×10^{-4}	6.3×10^{-5}	2.3×10^{-5}	260

TABLE 2. The convergence of the present solution $\Delta \boldsymbol{u}$ to the standard $O(N^2 N_\triangle^2)$ solution $\Delta \boldsymbol{u}_{ex}$ as $\varepsilon \to 0$, in the single-layer test for $c = 0.5$, $N = 200$, $N_\triangle = 1280$.

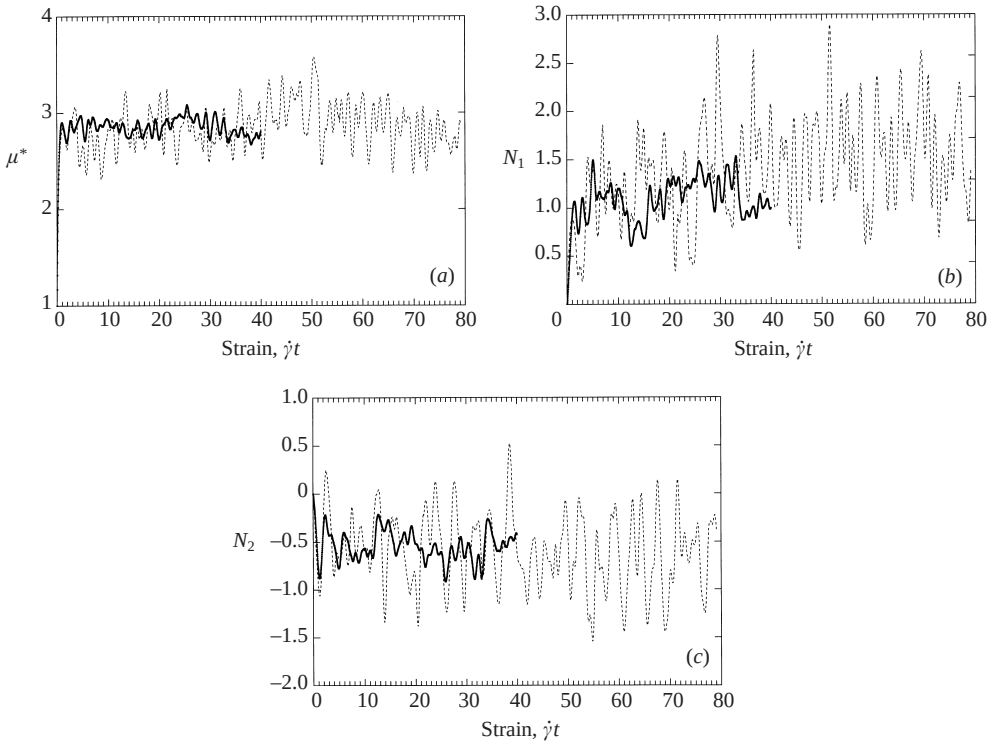

FIGURE 6. The trajectories of the dimensionless effective viscosity (a), and first (b) and second (c) normal stress differences vs. strain at $c = 0.5$, $\lambda = 1$, $Ca = 0.05$ and $N_\triangle = 1280$ for $N = 10$ (dashed lines) and $N = 100$ (solid lines) drops. A second-order Runge–Kutta scheme was used with step $\dot{\gamma}\Delta t = 0.0045$.

c), we integrated to strains $\dot{\gamma}t \sim 28$–45 for $N = 50$–200 and to $\dot{\gamma}t \sim 50$–80 for $N = 10$. Constant-strain steps of 0.0025, 0.00375, 0.0045, 0.01, 0.0135, 0.010, and 0.02 were used for $Ca = 0.025$, 0.0375, 0.05, 0.1, 0.15, 0.2, and 0.25–0.3, respectively. Second-order and first-order Runge–Kutta time integration schemes were employed for $Ca \geqslant 0.05$ and $Ca \leqslant 0.0375$, respectively (see below for the analysis of time integration errors); 1280 (for $Ca \geqslant 0.05$) or 1500 (for $Ca \leqslant 0.0375$) triangular elements per drop were used. An initial transient part of every trajectory ($\mu^*(\dot{\gamma}t)$, $N_1(\dot{\gamma}t)$, or $N_2(\dot{\gamma}t)$) was always excluded from averaging. The bounds on the cutoff strain γ_{cutoff} (often, the first two pronounced extrema of μ^*, N_1, or N_2) are usually obvious from the graphical analyses (e.g. see figures 6 and 7); to remove ambiguity, γ_{cutoff} was determined within these bounds to minimize the dispersion of partial averages over the four remaining strain intervals of equal length. This dispersion was also used for a rough estimation of the statistical error. Many results in figure 8 were double-checked starting from different random initial configurations; the discrepancies are consistent with the error estimates along a single trajectory. The direct boundary-integral code used for $N = 10$ is the same as we used to validate our economical method in table 2 (except that a faster, linear interpolation for the smooth part $\mathbf{G}_1$ of Green's function was employed on a coarser mesh $31 \times 31 \times 31$ in V, with these changes giving negligible errors for the purposes of comparisons in figure 8).

With $N \sim 10^2$, the absolute statistical errors in figure 8(a–c) are as small as 0.01 for $\langle \mu^* \rangle$ and 0.01–0.02 for $\langle N_1 \rangle$ and $\langle N_2 \rangle$ at $Ca = 0.2$, but can grow to 0.02 for

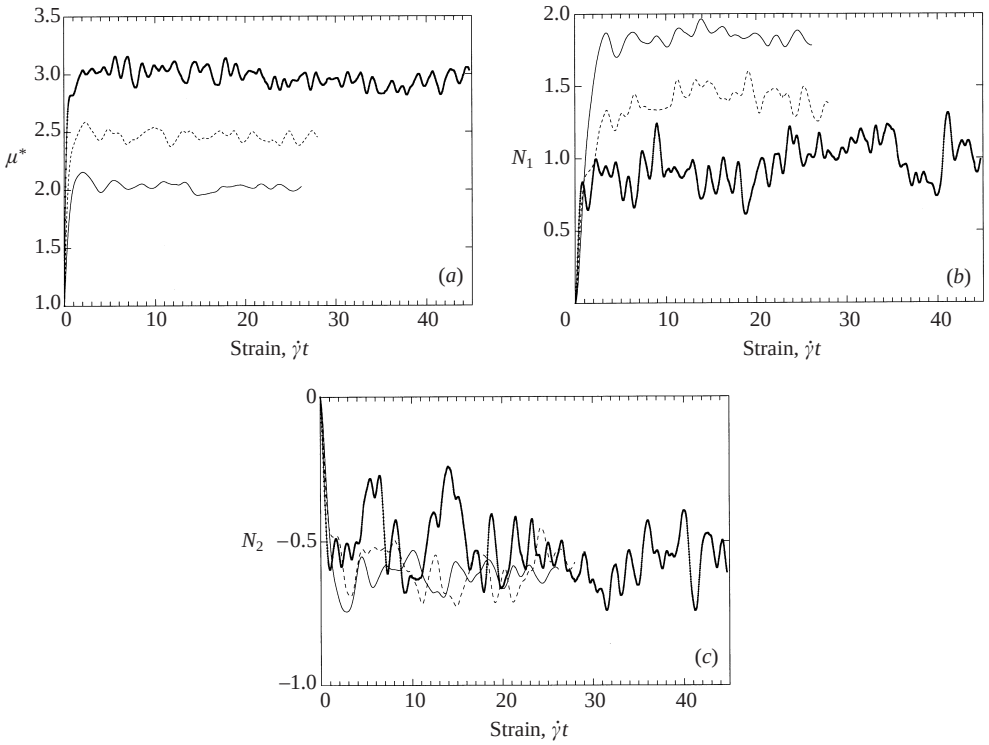

FIGURE 7. The trajectories of the dimensionless effective viscosity (a), and first (b) and second (c) normal stress differences for $c = 0.5$, $\lambda = 1$, $N_\triangle = 1280$–1500 and $N = 200$, with $Ca = 0.0375$ (thick lines), 0.1 (dashed lines) and 0.2 (thin solid lines). The simulation for $Ca = 0.25$ behaves similarly to that for $Ca = 0.2$ and is not shown.

$\langle\mu^*\rangle$ and 0.03–0.04 for $\langle N_1\rangle$ and $\langle N_2\rangle$ at the smallest capillary numbers, due to the increased dispersion of data as $Ca \to 0$ (figure 7). For $N = 10$, the statistical errors may be slightly higher. A few results (e.g. $\langle N_1\rangle$ and $\langle N_2\rangle$ for $N = 10$ and $Ca = 0.025$) with poor statistical convergence have been removed from figure 8. The cutoff strains γ_{cutoff} are typically from 2.5 to 5; the trajectory of N_1 in figure 6(b) represents a very unusual case with a much longer relaxation time ($\gamma_{\text{cutoff}} \sim 14$). The relaxation time is also larger for special initial conditions (see below) and for drops close to breakup. The latter is the case for $Ca = 0.3$ at $c = 0.5$ and $\lambda = 1$, and the steady-state viscosity $\langle\mu^*\rangle$ for $N = 100$ is noticeably higher than for $N = 10$ (figure 8a), probably due to the confining effect of the periodic box on drop deformation in small systems. At $Ca = 0.2$ and 0.1, the values of $\langle\mu^*\rangle$ for $N = 50$, 100, and 200 show excellent convergence, while the result for $N = 10$ at $Ca = 0.2$ still noticeably underestimates the viscosity. The convergence of $\langle\mu^*\rangle$ for $N = 100$ and 200 remains excellent at $Ca = 0.0375$. A close agreement between the viscosities for small ($N = 10$) and large systems at $Ca = 0.1$ and 0.05 is fortuitous, since the approximation $N = 10$ seriously underestimates $\langle\mu^*\rangle$ at a smaller capillary number $Ca = 0.025$. In all cases, a shear thinning effect is observed, as increasing Ca allows the drops to slide more easily past each other with larger deformation.

In general, figure 8(a) shows that small systems ($N \sim 10$) are inadequate for calculating $\langle\mu^*\rangle$ at high concentrations, underestimating the viscosity for large deformations and failing to predict the steep rise of $\langle\mu^*\rangle$ at $Ca \to 0$. Comparison of

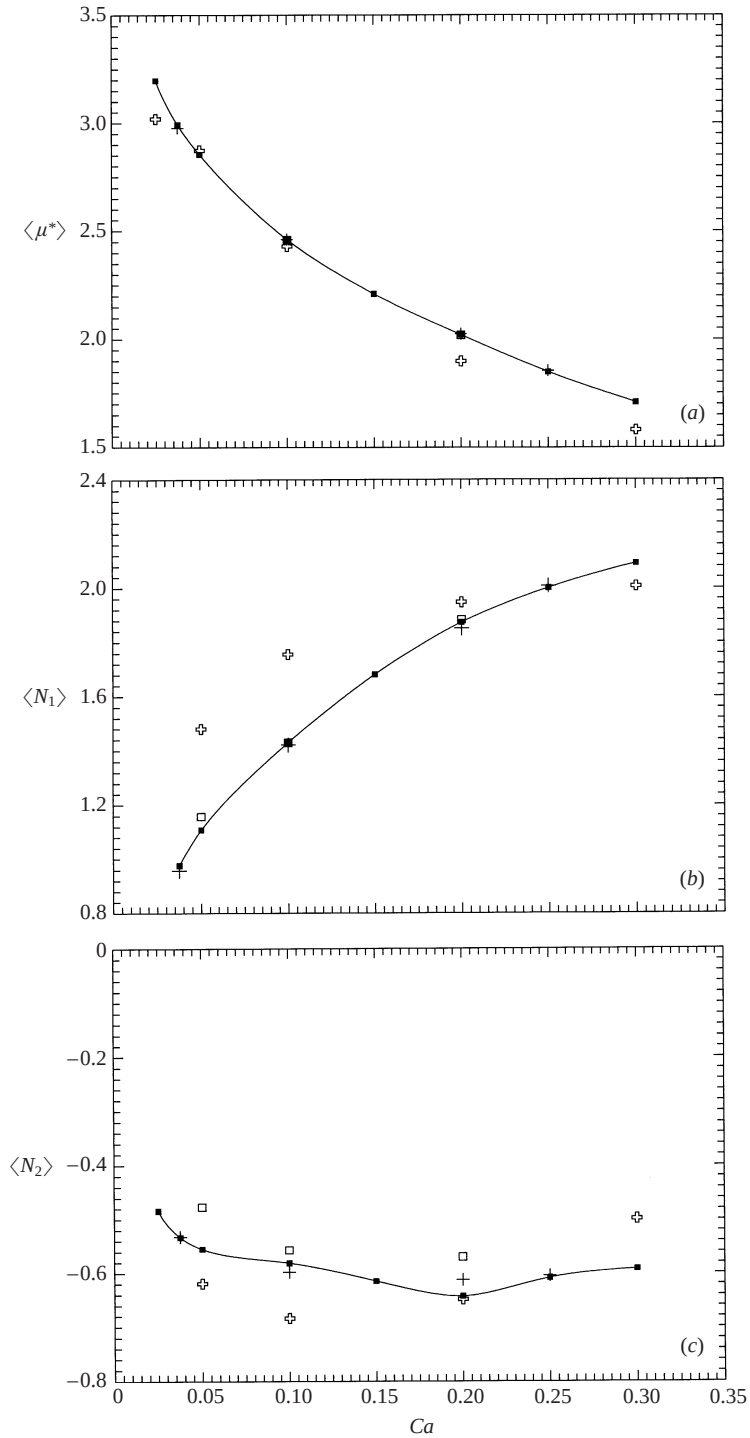

FIGURE 8. The N-dependence of the steady-state dimensionless effective viscosity (a), and first (b) and second (c) normal stress differences for $c = 0.5$, $\lambda = 1$, $N_{\triangle} = 1280$–1500 and different Ca. Open crosses are for $N = 10$, open squares are for $N = 50$, dark squares are for $N = 100$, and plus symbols are for $N = 200$.

the first normal stress difference $\langle N_1 \rangle$ for small and large systems (figure 8*b*) shows more dramatic deviations. At $Ca = 0.3$, a small system ($N = 10$) underestimates $\langle N_1 \rangle$, which is believed, again, to be a confining effect of the periodic box on drop deformation, since N_1 is quite sensitive to the aspect ratio. At $Ca = 0.2$, the values of $\langle N_1 \rangle$ for $N = 50$, 100, and 200 show excellent convergence, while the $N = 10$ approximation starts overestimating $\langle N_1 \rangle$, probably because multibody effects on N_1 become more important than the effect of drop deformation. The convergence of $\langle N_1 \rangle$ for $N = 50$, 100, and 200 remains excellent for $Ca = 0.1$, while the small system ($N = 10$) overestimates $\langle N_1 \rangle$ by about 23%. At $Ca = 0.05$, the results for $N = 50$ and 100 differ by only 4.5%, while the small system ($N = 10$) overpredicts $\langle N_1 \rangle$ almost 1.5-fold. The results for $N = 100$ and 200 remain in a close agreement for a smaller capillary number of $Ca = 0.0375$ (figure 8*b*). Except for small Ca, the positive first normal stress difference is comparable to the shear stress in magnitude.

For the second normal stress difference, $\langle N_2 \rangle$, the N-dependence may be most complicated and non-monotonic (figure 8*c*). At $Ca = 0.3$, the $N = 10$ approximation underestimates $|\langle N_2 \rangle|$ by about 16% compared to the result for $N = 100$. For $Ca = 0.1$, in contrast, the small system ($N = 10$) overpredicts $|\langle N_2 \rangle|$ by about 14%, compared to the result for $N = 200$; these deviations exceed the statistical errors. Although the convergence is less obvious in figure 7(*c*), we note that the discrepancy between $\langle N_2 \rangle$ for $N = 100$ and 200 is within 0.025 (and less than 1.5% of the shear stress $\langle \mu^* \rangle$), while the difference between the results for $N = 10$ and 200 is observed to reach 0.09. Unfortunately, at $Ca \to 0$, $\langle N_2 \rangle$ is almost inevitably subject to some relatively large statistical error, which complicates the analysis. Nevertheless, the results in figure 8(*c*) confirm the importance of using large systems ($N \geqslant O(10^2)$) in rheological simulations at high concentrations. The second normal stress difference is negative and, except for small Ca, much smaller in magnitude than the first normal stress difference.

For matching viscosities $\lambda = 1$, we have also systematically studied the steady-state viscometric functions $\langle \mu^* \rangle$, $\langle N_1 \rangle$, and $\langle N_2 \rangle$ at other concentrations, from 30% to 55% by volume, and different capillary numbers (figure 9*a–c*). Strains of 25–30 for moderate and of 30–45 for small capillary numbers were used. At $c = 0.55$, we evaluated the viscosity $\langle \mu^* \rangle$ only, with a statistical error of ± 0.02–0.03 (except for $Ca = 0.025$, see below); reliable averaging of the normal stress differences may require even longer runs than shown in figure 10 in this case of very high concentration, especially for small capillary numbers. At $Ca \geqslant 0.05$, from 1280 (for $c \leqslant 0.5$) to 1500 (for $c = 0.55$) triangular elements per drop and second-order Runge–Kutta integration were employed, while for $Ca \leqslant 0.0375$, we used finer triangulations ($N_\triangle = 1500$ for $c \leqslant 0.5$ and $N_\triangle = 2160$ for $c = 0.55$) and the first-order Euler time integration scheme. At 55% volume fraction, strain steps had to be small (from 0.002 for $Ca = 0.025$ to 0.01 for $Ca = 0.2$); in contrast, much larger steps could be used at $c = 0.3$ (from 0.0046 at $Ca = 0.025$ to 0.035 at $Ca = 0.3$). From stability considerations, at any given concentration, the strain step obeys the scalings $\dot{\gamma}\Delta t \sim N_\triangle^{-1/2}$ and, as $Ca \to 0$, $\dot{\gamma}\Delta t \sim Ca$, making the calculations for drops with small deformations most difficult; for drops with large deformations, the strain step was chosen to be weakly dependent on Ca. The effect of time integration errors on $\langle \mu^* \rangle$, $\langle N_1 \rangle$, and $\langle N_2 \rangle$ is surprisingly weak, even when the Euler scheme is used (see below). For $c = 0.4$ and 0.45, the statistical errors of $\langle \mu^* \rangle$, $\langle N_1 \rangle$, and $\langle N_2 \rangle$ are similar to those for $c = 0.5$ (see above), but for $c = 0.3$ they are much smaller (within ± 0.01). At $c \leqslant 0.4$, the effect of the system size is smaller than for $c = 0.5$ (figure 8); in particular, at $c = 0.4$ and $\lambda = 1$, the results $\langle \mu^* \rangle = 1.577 \pm 0.006$, $\langle N_1 \rangle = 1.459 \pm 0.004$, and $\langle N_2 \rangle = -0.426 \pm 0.007$ for

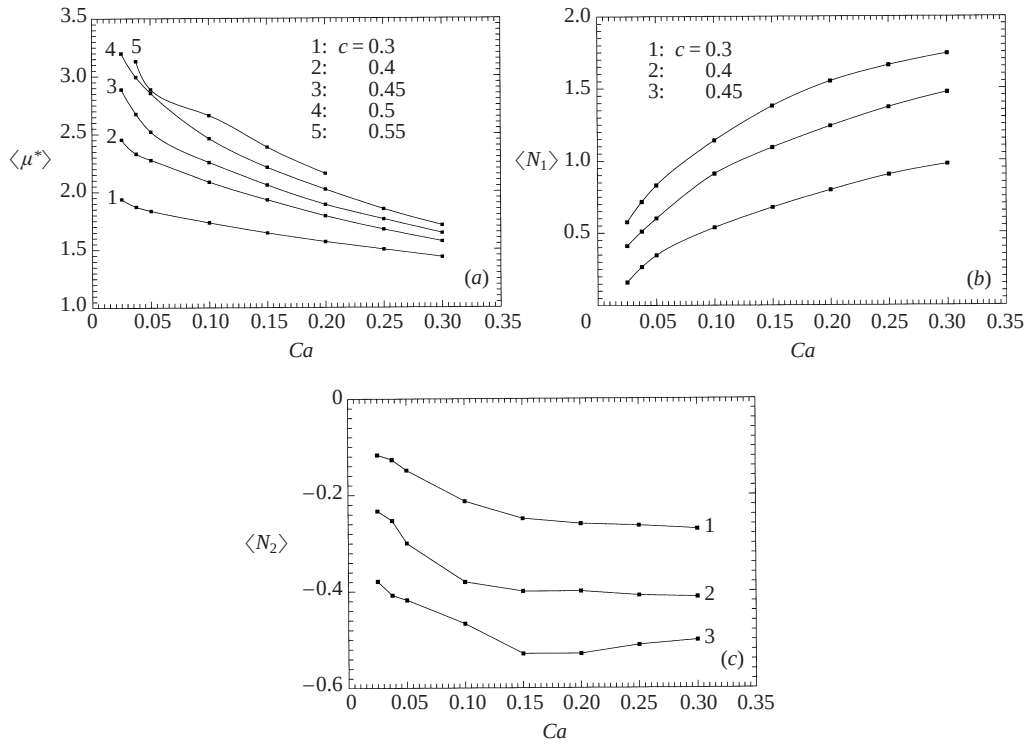

FIGURE 9. Steady-state results for the dimensionless effective viscosity (a), and first (b) and second (c) normal stress differences at $\lambda = 1$ and different concentrations c and capillary numbers, with $N_\triangle = 1280$–2160 and $N = 50$–100. At $c = 0.5$, the results for N_1 and N_2 are given in figure 8.

$Ca = 0.3$ and $\langle\mu^*\rangle = 2.286 \pm 0.009$, $\langle N_1\rangle = 0.618 \pm 0.017$, and $\langle N_2\rangle = -0.301 \pm 0.005$ for $Ca = 0.05$ obtained with $N = 100$ were fully reproduced, within statistical errors, by a calculation using 50 drops. For this reason, we used $N = 50$ in the calculations for figure 9 at $c = 0.3$ and 0.4, and $N = 100$ only at $c \geqslant 0.45$. Finally, as a check of triangulation errors, the results $\mu^* = 1.434 \pm 0.006$, $N_1 = 0.976 \pm 0.005$, and $N_2 = -0.271 \pm 0.004$ for $c = 0.3$, $\lambda = 1$, $Ca = 0.3$, and $N_\triangle = 1280$ compare well with $\mu^* = 1.444 \pm 0.004$, $N_1 = 0.963 \pm 0.009$, and $N_2 = -0.276 \pm 0.005$ obtained using 720 triangular elements per drop. It was also found for these c, λ, and Ca that the BPS method of paper I for normals and curvatures used in all the present calculations improves the convergence for $\langle\mu^*\rangle$ and $\langle N_2\rangle$ with respect to triangulations, but slightly slows down the convergence for $\langle N_1\rangle$ compared to the best-paraboloid algorithm (Zinchenko *et al.* 1997).

The most interesting observation from figure 9(a) is a sharp dependence of the emulsion viscosity on Ca at high concentrations $c = 0.45$ and 0.5, so that most of the shear thinning occurs for drops with only small deformation. This observation poses an interesting question about the behaviour of $\mu^*(Ca)$ for small Ca. In the phenomenological theory of simple (non-Newtonian) liquids (e.g. Astarita & Marrucci 1974), assuming certain 'smoothness hypotheses', the constitutive equation for slow flows is shown to be of Rivlin–Ericksen (1955) type. This general form is, indeed, confirmed by a small-deformation analysis of a single drop in a linear flow (Frankel & Acrivos 1970; Barthès-Biesel & Acrivos 1973); in particular, the viscosity of dilute emulsions turns out to be an analytical function of small Ca (and expandable

in even powers of Ca). Unfortunately, no such microstructural justification of the Rivlin–Ericksen theory exists for an emulsion of *interacting* drops. Even if the Rivlin–Ericksen theory is applicable to highly concentrated emulsions, the range of validity of the Rivlin–Ericksen expansion is limited to very small Ca, as suggested by our results in figure 9(a).

Also of interest in figure 9(a) is a qualitative change in the viscosity behaviour at very high concentrations. Namely, at $Ca = 0.05$ the emulsion viscosity undergoes only a very small increase, as the concentration is increased from 50% to 55%. This change in the viscosity is much smaller than at $Ca = 0.1$. The viscosity becomes a stronger function of concentration, however, when Ca is decreased to 0.0375. This seemingly abnormal behaviour cannot be explained by small statistical errors in our viscosity calculations for $Ca \geqslant 0.0375$ (figure 10). Besides, the approximation $N = 100$, which is excellent for μ^* at $c = 0.5$ (figure 8a), is therefore believed to have sufficient accuracy at $c = 0.55$, at least for $Ca \geqslant 0.0375$. Most likely, the results in figure 9(a) indicate the existence of the phase transition in a sheared emulsion to an ordered state at high concentrations. At $c = 0.55$ and $Ca \ll 0.0375$, the average viscosity $\langle \mu^* \rangle$ is expected to become an even stronger function of Ca, but it was not possible to calculate $\langle \mu^* \rangle$ in this range due to ergodic difficulties: the trajectory of $\mu^*(\dot{\gamma}t)$ for $Ca = 0.025$ (figure 10) has two distinct quasi-stationary levels (about 3.53 and 3.14), and without further extensive calculations, it is impossible to determine the frequency of transitions between the two probably dynamically metastable states. This two-level behaviour is a known general phenomenon in phase transition simulations in statistical physics and can make time averaging, unfortunately, a prohibitive task. For thermodynamical systems of 'hard spheres' the phase transition to an ordered state is believed to occur in the range $0.49 \leqslant c \leqslant 0.55$ (e.g. Hansen & McDonald 1976). Our results indicate that the phase transition concentrations for a sheared emulsion are similar to those for a 'hard-sphere' dispersion, but not necessarily the same, and they also depend on the capillary number; ergodic difficulties and transitional behaviour were never observed for large deformations. To elucidate this difficult issue of phase transition, the structural analysis of configurations would be instructive. However, to observe the structural changes, much larger simulations (with $N \sim 10^3$) may be required, which were not attempted in the present work.

The positive dimensionless first normal stress difference, $\langle N_1 \rangle$, is also a strong function of Ca at high concentrations and sharply decreases as $Ca \to 0$ (figure 9b); the asymptotic behaviour, however (in particular, the possibility of $\langle N_1 \rangle$ changing sign) remains an open question. Unfortunately, accurate numerical simulations for even smaller values of Ca than those in figure 9(b) would be quite difficult. Unlike for the viscosity $\langle \mu^* \rangle$, there are no general mechanical principles to predict the signs of $\langle N_1 \rangle$ and $\langle N_2 \rangle$.

The dimensionless second normal stress difference, $\langle N_2 \rangle$, is found to be negative and is at least several times smaller than the dimensionless shear stress $\langle \mu^* \rangle$ (figure 9c). Although it is quite difficult to accurately determine the slopes of $\langle N_2 \rangle$ vs. Ca in figure 9(c) at small Ca due to statistical errors, the limiting values of $\langle N_2 \rangle$ at $Ca = 0$ are expected to remain negative (see also later figures). Non-zero values of $\langle N_2 \rangle$ at $Ca = 0$ would indicate that, in physical units, the second normal stress difference is a linear (not a quadratic) function of the shear rate $|\dot{\gamma}|$ at $\dot{\gamma} \to 0$, which is the effect of drop interactions; such a behaviour cannot be described by a Rivlin–Ericksen phenomenological equation.

Loewenberg & Hinch (1996) and Loewenberg (1998) were the first to study the rheological properties of three-dimensional disordered emulsions of interacting deformable

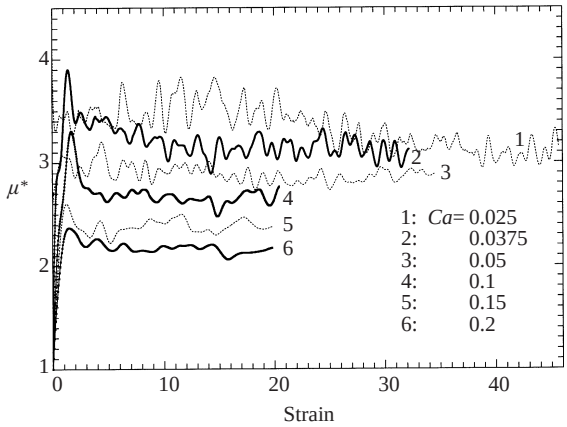

FIGURE 10. The trajectories of the dimensionless effective viscosity for $c = 0.55$, $\lambda = 1$ and different Ca, with $N = 100$ and $N_\triangle = 1500$–2160. At $Ca = 0.025$, an initial condition from a steady state for a different capillary number was used; the average viscosity for this Ca could not be determined due to ergodic difficulties. At $Ca = 0.0375$, an initial metastable (i.e. insufficiently well-mixed) configuration of spheres slowed down relaxation to a steady state.

drops by numerical simulation. They used a direct, point-to-point boundary-integral implementation, with quadratic scalings in N and $N_\triangle$, and considered $N = 12$ drops with $N_\triangle = 320$ triangular elements per drop (or $N = 6$ with $N_\triangle = 720$) to simulate steady-state viscometric functions at volume fractions c up to 30%. Their results are in terms of particle stresses Σ_{12}^P, N_1^P, and N_2^P (denoted by Σ_{12}, N_1, and N_2 in Loewenberg & Hinch 1996) related to our μ^*, N_1, and N_2 by $\Sigma_{12}^P = Ca(\mu^* - 1)/c$, $N_1^P = Ca\ N_1/c$ and $N_2^P = Ca\ N_2/c$. At $c = 0.3$ and $Ca \geqslant 0.05$, our $\langle \Sigma_{12}^P \rangle$, $\langle N_1^P \rangle$ and $\langle N_2^P \rangle$ (which can be derived from our figure 9) are in approximate (sometimes, very good) agreement with those of Loewenberg & Hinch (1996) and Loewenberg (1998), although the deviations are larger than expected for strong deformations ($Ca \sim 0.3$), reaching 20–24% for all $\langle \Sigma_{12}^P \rangle$, $\langle N_1^P \rangle$ and $\langle N_2^P \rangle$. The main qualitative difference is that our particle shear stress, $\langle \Sigma_{12}^P \rangle$, is always a monotonically increasing function of Ca, including the case of 30% volume concentration. We believe that the use of limited triangulations in the earlier papers, in combination with a contour integration method for curvatures and normals (which is known to contain difficulties) have slowed down the convergence to the exact solution. At $c = 0.3$, the approximation $N = 12$ is likely to suffice for intermediate Ca (since single-drop contributions to the particle stress still prevail) but, nevertheless, may also have some effect at large deformations, when the drop lengths are comparable with the size of the periodic box.

For a substantial viscosity contrast between the drops and the medium, the calculations are considerably more difficult and, at least, several times more computationally expensive than for $\lambda = 1$. In the simulations below, we have chosen $\lambda > 1$ to demonstrate stronger effects of the capillary number and concentration on the viscometric functions, compared to the case of $\lambda < 1$. Figure 11 presents a typical snapshot of our dynamical simulation with $\lambda = 3$, $c = 0.55$, $Ca = 0.1$, $N = 100$, and $N_\triangle = 1500$ at the steady-state strain of $\dot{\gamma}t = 6.38$; only 100 drops with centres in $(0, 1)^3$, an initial periodic cell, are shown. The whole simulation was done from a well-mixed state of spherical drops at $t = 0$ to $\dot{\gamma}t \approx 11$ by the Euler scheme with a constant-strain step $\dot{\gamma}\Delta t = 0.003$. For the snapshot in figure 11, the preiterative part took 130 s on a DEC 600au, including 5 s for normal and curvature calculations, 103 s for the

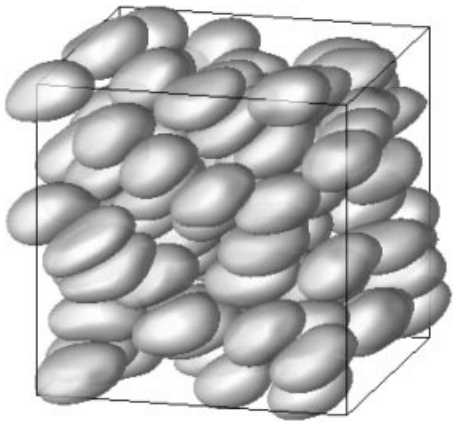

FIGURE 11. A snapshot of the dynamical simulation for $c = 0.55$, $\lambda = 3$, $Ca = 0.1$, $N = 100$ and $N_\triangle = 1500$ at the steady-state strain of $\dot{\gamma}t = 6.38$. The centres of 100 independent drops have been mapped into $(0,1)^3$, an initial periodic cell.

inhomogeneous terms (2.5) with all overheads (tabulation of far-field derivatives etc.) and 22 s to take part of the work (3.7) in the near-singularity subtractions out of iterations. After that, each velocity iteration took 99 s; for the steady state, typically five iterations per time step sufficed (with the convergence criterion as in § 2). As for the single layer (2.5), it was crucial to validate our relatively complicated hybrid scheme for the double-layer integrals (2.4). To this end, we compared, for the snapshot in figure 11, the excess velocity $\Delta\boldsymbol{u}(\boldsymbol{y}) = \boldsymbol{u}(\boldsymbol{y}) - \boldsymbol{u}_\infty(\boldsymbol{y})$ obtained by one iteration of (2.4) at different precisions ε with $\Delta\boldsymbol{u}_{\rm ex}(\boldsymbol{y}) = \boldsymbol{u}_{\rm ex}(\boldsymbol{y}) - \boldsymbol{u}_\infty(\boldsymbol{y})$ calculated in the same manner using the standard $O(N^2 N_\triangle^2)$ point-to-point summations for the double layer (2.4). In all these tests, we started from the same initial approximation $\boldsymbol{u}(\boldsymbol{x})$ provided by the previous time step, and used the same $\boldsymbol{F}(\boldsymbol{y})$ fixed from our hybrid calculation with $\varepsilon = 10^{-3}a$, since the single-layer part of our code was already validated (table 2). In the point-to-point scheme, we used, again, the quadratic Taylor approximation from the $91 \times 91 \times 91$ mesh in V to interpolate the smooth part $\boldsymbol{\tau}_1$ of the stresslet. Table 3 presents the deviations $\delta_i(\Delta\boldsymbol{u}, \Delta\boldsymbol{u}_{\rm ex})$ defined in (5.2) and the CPU times (in s) on a DEC 600au for one iteration by the present method vs. the precision parameter ε (§ 4), for drop partitioning into blocks (i) enabled (with a total of 179 blocks) and (ii) disabled. The convergence ($\delta_i \to 0$ as $\varepsilon \to 0$) to the point-to-point scheme validates the double-layer part of our code. At $\varepsilon = 10^{-3}a$ and drop partitioning enabled (as in dynamical simulations for figure 11), one velocity iteration by our method is 106 times faster than by the standard point-to-point scheme, even with the simplest, linear interpolation for $\boldsymbol{\tau}_1$ in the standard method. This gain is even higher when the volume fraction and/or drop deformation decrease.

For $c = 0.45$, $\lambda = 3$, and $N = 100$, we have studied systematically the effects of the triangulation and time-step integration errors on the viscometric functions (with other conditions being equal, the triangulation effects for $\lambda = 1$ are expected to be smaller than those for $\lambda = 3$, since the double-layer integrals are most sensitive to discretization errors). In figure 12(a), the trajectories of μ^*, N_1, and N_2 are shown for $Ca = 0.2$ with two triangulations $N_\triangle = 1500$ (solid lines) and $N_\triangle = 720$ (dashed lines) starting from the same random configuration of spherical drops. The second-order Runge–Kutta scheme was used, with strain steps $\dot{\gamma}\Delta t = 0.016$ and 0.023 for $N_\triangle = 1500$ and 720, respectively; on average, five velocity iterations per 1/2 step

	With drop partitioning				Without drop partitioning			
ε	δ_1	δ_2	δ_3	CPU time (s)	δ_1	δ_2	δ_3	CPU time (s)
$10^{-2}a$	1.8×10^{-2}	5.0×10^{-3}	1.3×10^{-3}	78	1.3×10^{-2}	2.4×10^{-3}	7.1×10^{-4}	101
$3 \times 10^{-3}a$	4.3×10^{-3}	1.8×10^{-3}	5.3×10^{-4}	89	4.0×10^{-3}	1.1×10^{-3}	3.2×10^{-4}	113
$10^{-3}a$	1.8×10^{-3}	6.8×10^{-4}	1.8×10^{-4}	99	1.6×10^{-3}	2.6×10^{-4}	8.2×10^{-5}	136
$3 \times 10^{-4}a$	6.4×10^{-4}	2.3×10^{-4}	6.5×10^{-5}	121	6.2×10^{-4}	9.0×10^{-5}	2.7×10^{-5}	159
$10^{-4}a$	2.2×10^{-4}	8.3×10^{-5}	2.4×10^{-5}	141	2.0×10^{-4}	3.4×10^{-5}	9.9×10^{-6}	186
$10^{-5}a$	2.3×10^{-5}	1.0×10^{-5}	3.3×10^{-6}	194	1.9×10^{-5}	4.4×10^{-6}	2.2×10^{-6}	260

TABLE 3. The convergence of the present solution $\Delta \boldsymbol{u}$ to the standard $O(N^2 N_\triangle^2)$ solution $\Delta \boldsymbol{u}_{\mathrm{ex}}$, as $\varepsilon \to 0$, in the double-layer test (one velocity iteration) for $c = 0.55$, $\lambda = 3$, $Ca = 0.1$, $N = 100$, and $N_\triangle = 1500$.

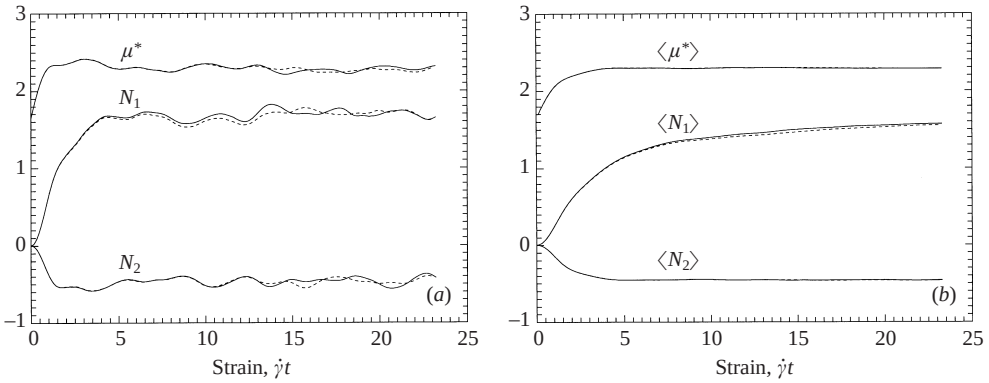

FIGURE 12. (*a*) The trajectories of μ^*, N_1 and N_2 for $c = 0.45$, $\lambda = 3$, $Ca = 0.2$, $N = 100$, and two runs $N_\triangle = 1500$, $\dot{\gamma}\Delta t = 0.016$ (solid lines) and $N_\triangle = 720$, $\dot{\gamma}\Delta t = 0.023$ (dashed lines), starting from identical initial conditions; (*b*) the same as (*a*), but for the average values $\langle\mu^*\rangle_{\dot{\gamma}t}$, $\langle N_1\rangle_{\dot{\gamma}t}$ and $\langle N_2\rangle_{\dot{\gamma}t}$ in the strain interval $[0,\ \dot{\gamma}t]$.

sufficed. The coarse and fine solutions practically coincide up to $\dot{\gamma}t \approx 13$ for μ^* and N_2 (probably due to convergence acceleration achieved by using BPS) and up to $\dot{\gamma}t \approx 5$ for N_1. Fortunately, the inevitable divergence of individual trajectories at large strains does not preclude accurate calculation of the steady-state levels $\langle\mu^*\rangle$, $\langle N_1\rangle$, and $\langle N_2\rangle$. Indeed, the comparison of the average values $\langle\mu^*\rangle_{\dot{\gamma}t}$, $\langle N_1\rangle_{\dot{\gamma}t}$, and $\langle N_2\rangle_{\dot{\gamma}t}$ in the strain interval $[0,\ \dot{\gamma}t]$ (figure 12*b*) between the two solutions shows much smaller differences which do not accumulate as $\dot{\gamma}t \to \infty$. The discrepancies between the stationary levels for the crude and fine solutions are estimated as 0.1%, 1.7%, and 0.4% for $\langle\mu^*\rangle$, $\langle N_1\rangle$, and $\langle N_2\rangle$, respectively.

In a more difficult case $Ca = 0.05$, we have studied the effects of triangulation and time step separately. In figure 13(*a*), the Euler scheme with the strain step $\dot{\gamma}\Delta t = 0.002$ was used for two triangulations $N_\triangle = 1500$ (solid lines) and $N_\triangle = 720$ (dashed lines). Unlike for $Ca = 0.2$, individual trajectories randomize quickly, and the effect of triangulation is pronounced after just several units of strain (figure 13*a*). However, the average values of μ^*, N_1, and N_2 in a large interval $[0,\ \dot{\gamma}t]$ are much less sensitive to triangulation (figure 13*b*) than are the individual trajectories. As $\dot{\gamma}t \to \infty$, the discrepancies between $\langle\mu^*\rangle_{\dot{\gamma}t}$, $\langle N_1\rangle_{\dot{\gamma}t}$, and $\langle N_2\rangle_{\dot{\gamma}t}$ for the crude and fine solutions are estimated as 1% for μ^* and about 2% for N_1 and N_2. Increasing the strain step to 0.004 in the simulation with $N_\triangle = 720$ has, surprisingly, a much smaller effect (figure 14*a*, *b*), even though the first-order Euler scheme is seemingly crude. Moreover, we regarded this scheme in the present simulations as the best choice at small Ca; indeed, to be advantageous, high-order time integration schemes would require much larger steps, prohibited by stability constraints. Finally, we considered the effect of the precision parameter ε on dynamical simulations, both for $Ca = 0.05$ and 0.2, by repeating the runs with $N_\triangle = 720$ using $\varepsilon = 0.003$ instead of 0.001, up to strains of 10; the effect of ε on individual trajectories was much less than the effect of the time step.

At $c = 0.45$, $\lambda = 3$, $N = 100$, and $N_\triangle = 1500$, we also studied two more capillary numbers, using Euler integration to $\dot{\gamma}t \sim 22$–23 with strain steps 0.005 and 0.0015 for $Ca = 0.1$ and 0.025, respectively (figure 15*a*–*c*). At $Ca = 0.025$, unfortunately, the data for normal stress differences are widely dispersed, with probable absolute statistical errors in $\langle N_1\rangle$ and $\langle N_2\rangle$ as big as ± 0.06 and ± 0.04, respectively. In figure 16*a*–*c*,

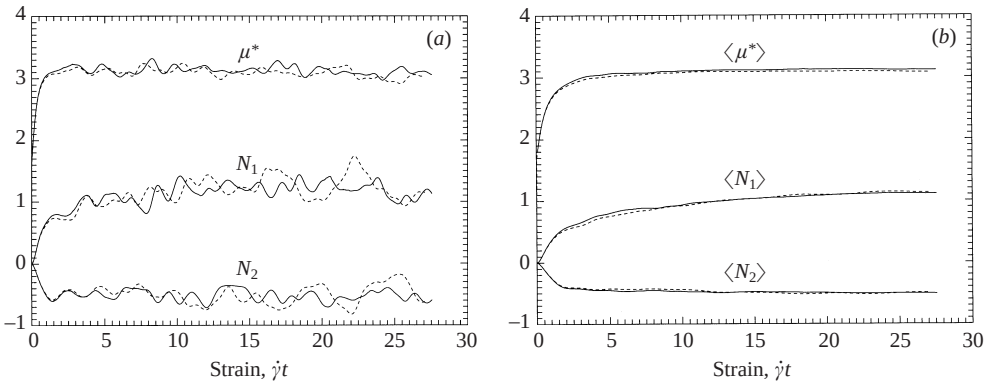

FIGURE 13. (*a*) The trajectories of μ^*, N_1 and N_2 for $c = 0.45$, $\lambda = 3$, $Ca = 0.05$, $N = 100$ and two triangulations $N_\triangle = 1500$ (solid lines) and 720 (dashed lines), with identical initial conditions and the same Euler strain step $\dot\gamma\Delta t = 0.002$. (*b*) the same as (*a*), but for the average values $\langle\mu^*\rangle_{\dot\gamma t}$, $\langle N_1\rangle_{\dot\gamma t}$ and $\langle N_2\rangle_{\dot\gamma t}$ in the interval $[0, \dot\gamma t]$.

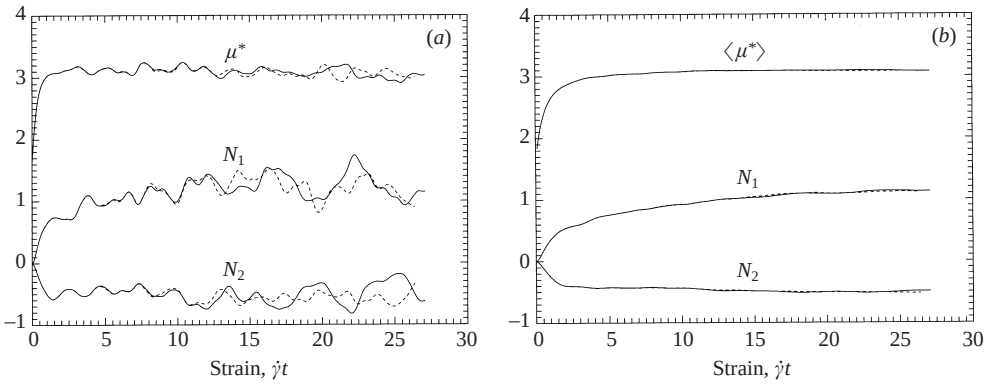

FIGURE 14. (*a*) The trajectories of μ^*, N_1 and N_2 for $c = 0.45$, $\lambda = 3$, $Ca = 0.05$, $N = 100$, $N_\triangle = 720$ and two different Euler time steps $\dot\gamma\Delta t = 0.002$ (solid lines) and 0.004 (dashed lines), with identical initial conditions; (*b*) the same as (*a*), but for the average values $\langle\mu^*\rangle_{\dot\gamma t}$, $\langle N_1\rangle_{\dot\gamma t}$ and $\langle N_2\rangle_{\dot\gamma t}$ in the interval $[0, \dot\gamma t]$.

the steady-state viscometric functions are shown vs. Ca for $\lambda = 1$ and 3 at 45% volume concentration. In figure 17*a–c*, the steady-state results for $\lambda = 1$, 2 and 5 are compared at 30% volume concentration. Although the effect of $N_\triangle$ on the steady-state results is small in all of our simulations, it was important to avoid an alternative of using too crude triangulations; otherwise, a run may not succeed to strains large enough for averaging. Even at $c = 0.3$, $\lambda = 5$ and $Ca = 0.05$, a run with $N_\triangle = 1280$ failed after several units of strain due to divergence of velocity iterations (despite the improvement in near-singularity subtraction, § 3), and we had to repeat the simulation with $N_\triangle = 2160$ to reach $\dot\gamma t = 20$. In other runs for figure 17 at $\lambda \neq 1$, $N_\triangle = 1280$ was used. Interestingly, for $\lambda = 5$, $|\langle N_2\rangle|$ behaves differently than for $\lambda = 1$ and 2, and is a monotonically decreasing function of Ca. Besides, it follows from figure 17(*b*) that $\langle N_1\rangle$, in general, is a non-monotonic function of $\lambda > 1$. For $c = 0.3$ and $\lambda = 2$, the particle stresses $\langle\Sigma_{12}^P\rangle$, $\langle N_1^P\rangle$ and $\langle N_2^P\rangle$, which can be derived from our figure 17(*a–c*), are in approximate agreement with the results calculated previously by Loewenberg

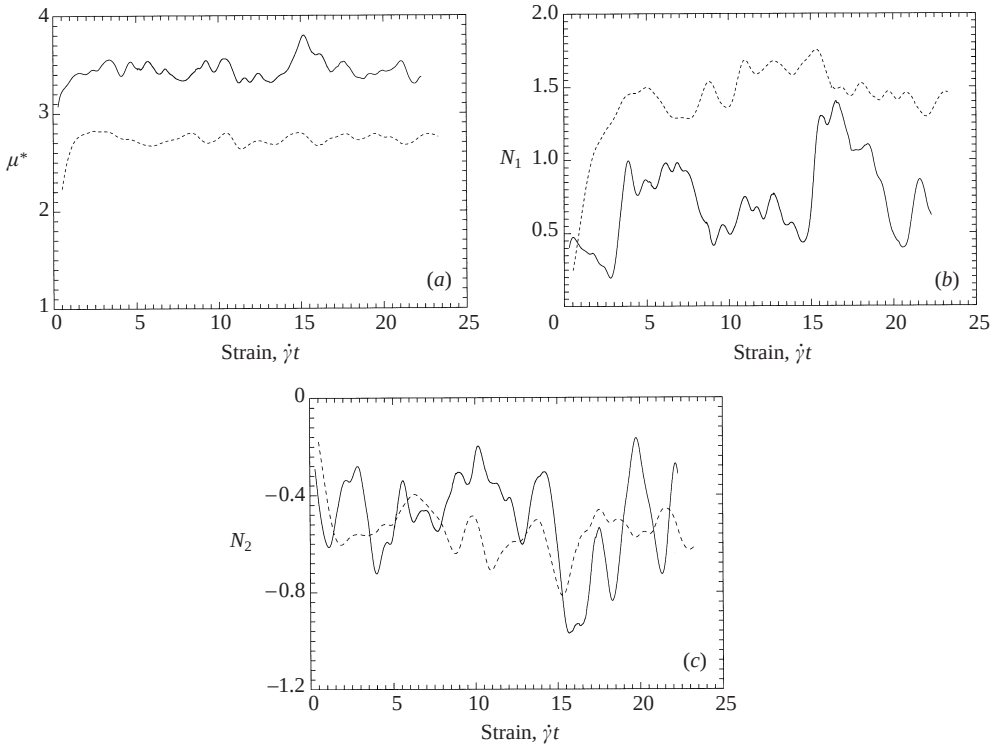

FIGURE 15. The trajectories of the dimensionless effective viscosity (*a*), and first (*b*) and second (*c*) normal stress differences for $c = 0.45$, $\lambda = 3$, $N = 100$, $N_\triangle = 1500$ and two capillary numbers $Ca = 0.1$ (dashed lines) and 0.025 (solid lines).

(1998), with the most noticeable deviation being a 30% difference in the large value of $\langle N_1^P \rangle$ at $Ca = 0.3$.

Finally, we ran some more limited dynamical simulations at $c = 0.55$, $\lambda = 3$, $N = 100$ and $N_\triangle = 1500$ for three capillary numbers of $Ca = 0.15$, 0.1 and 0.05 (figures 11 and 18). Smaller Ca would be very difficult to simulate. On the other hand, a run at $Ca = 0.2$ could not reach a steady state due to continued elongation and, probably, incipient breakup of individual drops. The simulated strains of $\dot{\gamma}t \sim 11$–15 were generally not enough for averaging N_1 and N_2, but allowed us to calculate the steady-state viscosities $\langle \mu^* \rangle = 2.96 \pm 0.02$, 3.37 ± 0.02 and 4.03 ± 0.01 for $Ca = 0.15$, 0.1 and 0.05, respectively. Again, the emulsion viscosity is a strong function of Ca, showing a distinct shear-thinning behaviour due to drop deformation. Interestingly, for the same $c = 0.55$ and Ca, the drops with $\lambda = 3$ experience somewhat larger average deformation than do $\lambda = 1$ drops (in the dilute limit, the trend would be the opposite). Increased drop deformation for $\lambda = 3$ helps to eliminate geometrical blockages and, presumably, shift the phase transition toward smaller capillary numbers, compared to the $\lambda = 1$ case (see figure 9*a*).

6. Conclusions

We have developed an efficient three-dimensional algorithm for hydrodynamical interaction of many deformable drops subject to shear flow at small Reynolds numbers with triply-periodic boundaries. The algorithm is a hybrid of the boundary-integral

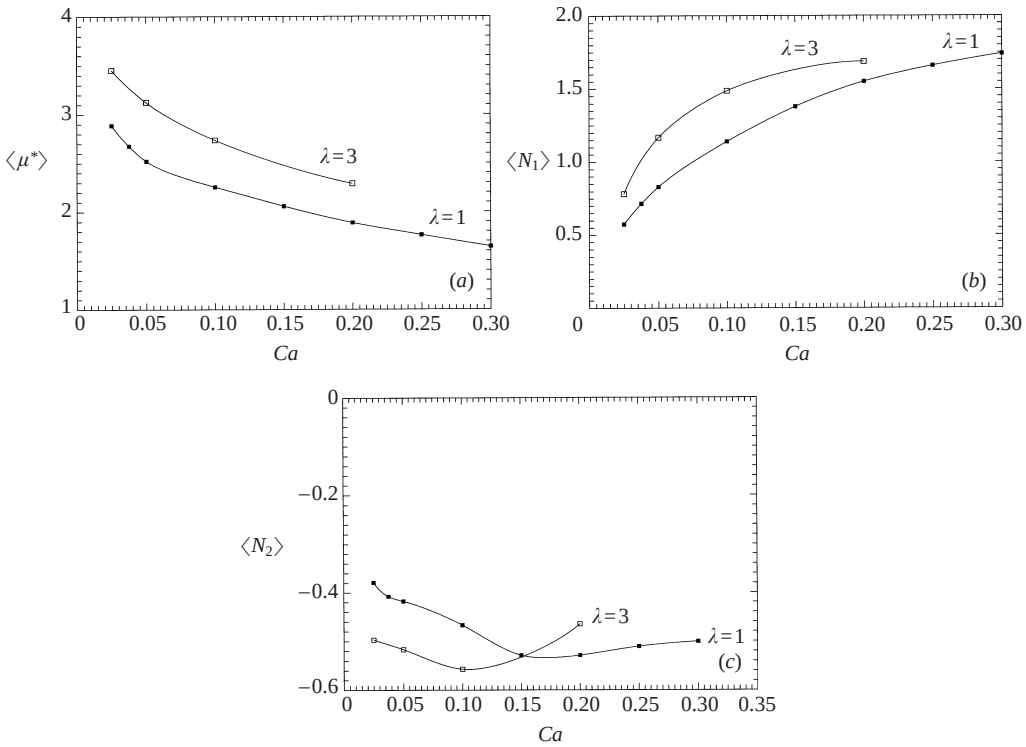

FIGURE 16. The steady-state viscometric functions (*a*) $\langle \mu^* \rangle$, (*b*) $\langle N_1 \rangle$ and (*c*) $\langle N_2 \rangle$ for $\lambda = 1$ and 3 at 45% drop volume fraction.

and economical multipole techniques and generalizes our previous method developed for sedimentation (Zinchenko & Davis 2000) for the case when the periodic cell evolves in a cyclic manner. In addition to new far-field calculation techniques, a crucial element is the method developed for near-singularity subtraction in the double-layer integrals, allowing long-time simulations at high concentrations with substantial viscosity contrast λ between the drops and the medium.

Using this method, long-time dynamical simulations for $N = 100$–200 disordered drops in steady shear with $N_\triangle = 1000$–2000 boundary elements per drop have been performed for drop volume fractions up to 55% and viscosity ratios up to $\lambda = 5$, to calculate the emulsion viscosity and normal stress differences by time averaging. The use of large N is essential at high concentrations. Small systems ($N \sim 10$) were found to give particularly large errors for normal stress differences and failed to predict a qualitatively correct behaviour of the emulsion viscosity. Since every run took $O(10^3$–$10^4)$ time steps, a direct $O(N^2 N_\triangle^2)$ point-to-point boundary-integral method would not be an option for these types of simulation. The present method is two orders of magnitude faster for $N \sim 10^2$ and $N_\triangle \sim 10^3$, without significant loss of precision, making such calculations feasible.

As discussed in Zinchenko & Davis (2000), our approach, although heavily based on multipoles, is not a 'fast multipole method (FMM)'; in particular, the familiar hierarchy of space decompositions by Cartesian grids (see Greengard & Rokhlin 1997 and references therein) is not used in our code. The FMM, although applicable in principle for multipole acceleration of the boundary-integral calculations for three-

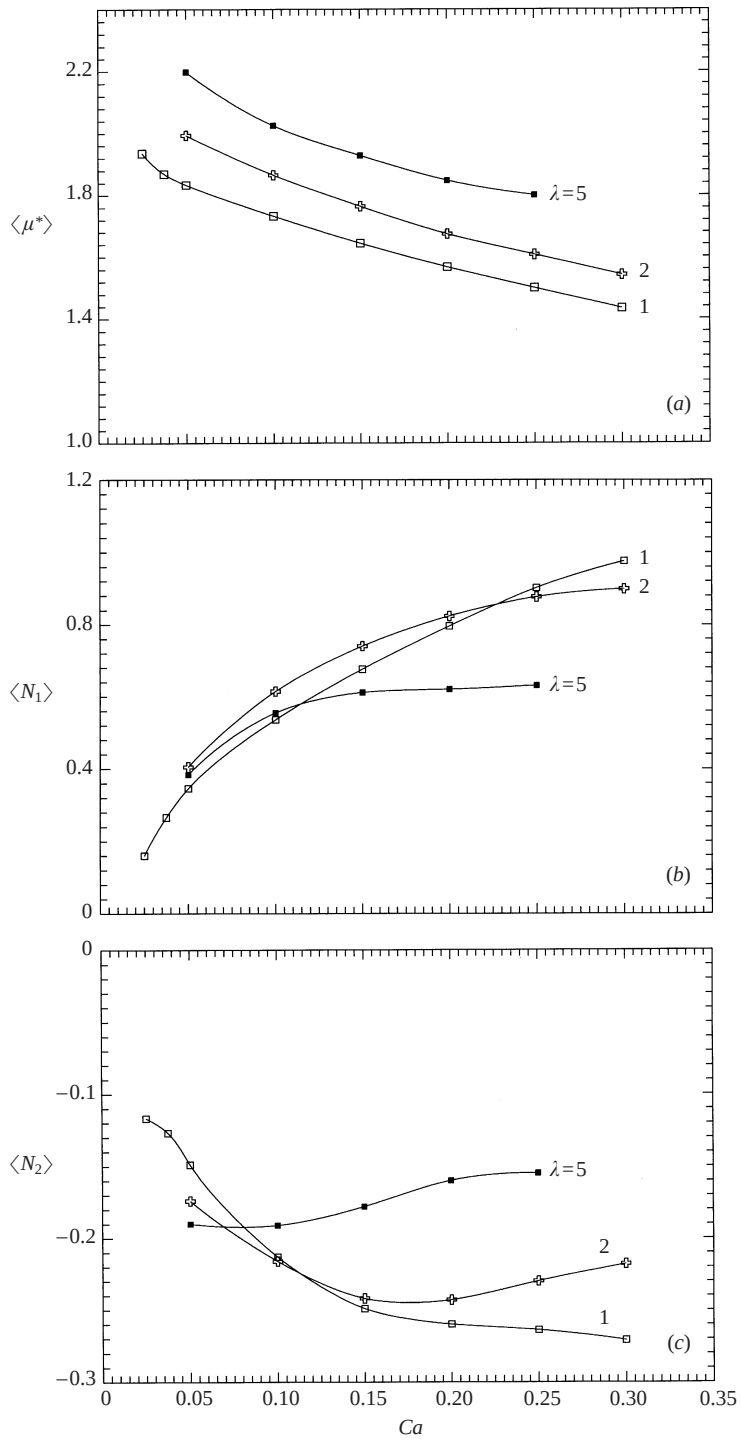

FIGURE 17. The steady-state viscometric functions (*a*) $\langle \mu^* \rangle$, (*b*) $\langle N_1 \rangle$ and (*c*) $\langle N_2 \rangle$ for $\lambda = 1$, 2, and 5 at 30% drop volume fraction and $N = 50$. Strains $\dot{\gamma} t = 25$–40 and 20–30 were used for $\lambda = 2$ and 5, respectively.

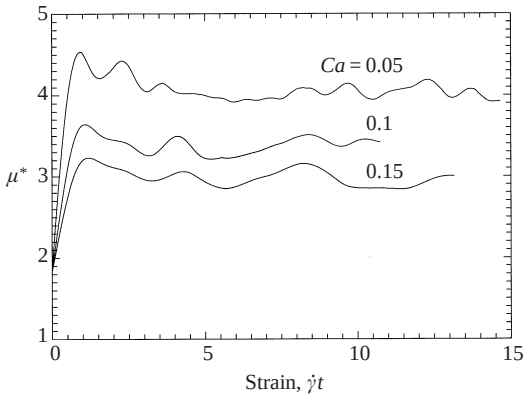

FIGURE 18. The trajectories of the dimensionless effective viscosity for $c = 0.55$, $\lambda = 3$, $N = 100$, $N_\triangle = 1500$ and different capillary numbers. The Euler scheme with steps $\dot{\gamma}\Delta t = 0.002$ and 0.003 is used for $Ca = 0.05$ and 0.1, respectively; the second-order Runge–Kutta scheme with $\dot{\gamma}\Delta t = 5.25 \times 10^{-3}$ is used for $Ca = 0.15$.

dimensional Stokes equations, has not been yet developed to a necessary stage to facilitate comparisons with our method in terms of performance and results.

At high concentrations, $c = 0.45$ and 0.5, the emulsion viscosity was found to have a very steep gradient at small capillary numbers, so that most of the shear thinning occurs for nearly non-deformable drops. The ratio of the second normal stress difference to the shear stress is observed to remain $O(1)$, as $Ca \to 0$, which is the effect of drop interactions; this behaviour could not be described by a hierarchy of phenomenological Rivlin–Ericksen constitutive equations at $Ca \to 0$. We have also found that the positive first normal stress difference scaled with the shear rate is a strong monotonically increasing function of Ca at small Ca. For $Ca \to 0$, accurate boundary-integral calculations, even accelerated by multipoles, would be prohibitively expensive.

Our results for viscometric functions also indicate the possible presence of a phase-transition phenomenon in a sheared emulsion at volume fractions of about 50–55% and small capillary numbers $Ca \leqslant 0.05$ at $\lambda = 1$. Higher viscosity ratio $\lambda = 3$ is expected to shift the phase transition towards smaller capillary numbers. To observe structural changes, however, even larger systems ($N \sim 10^3$) may be required, which were not investigated in the present work.

The present method and calculations can be extended in several ways. Time-dependent shear flow, or moderately polydisperse emulsions, would be the most straightforward generalizations. Also, an insoluble surfactant or thermocapillary effects could be incorporated using boundary-integral desingularization procedures developed for pairwise thermocapillary interactions (Rother, Zinchenko & Davis 2001). Simulation of the rheology of dense emulsions with an arbitrary history of deformation remains a major challenge.

Note that we advocate using gap-non-adaptive meshes with fixed topology in the present simulations, even at high drop volume fractions. Indeed, the existence of multiple near-contact zones around a drop, and an appreciable size of each zone can easily eliminate the advantages of gap adaptivity. This approach, however, is expected to have limitations in the most difficult ranges of very small (but finite) Ca, or high viscosity ratios $\lambda > O(10)$, when the solution is more lubrication sensitive.

Instead of partitioning of elongated drops into compact blocks in our method, it

may be more advantageous for $N \gg 1$ and large deformations to consider minimal spheroidal shells around drops and then use the tool of spheroidal harmonics; some encouraging related progress has been made recently in calculating the effective conductivity and stiffness of solid suspensions of disks by spheroidal harmonics (Kushch & Sangani 2000*a*, *b*). This prospective improvement of our multidrop technique is currently being investigated.

This work was supported by the National Aeronautics and Space Administration. Special thanks are extended to Mike Rother and Yingyuan Wu for assistance with some of the figures.

Appendix A. Mesh stabilization algorithm

A familiar difficulty in three-dimensional boundary-integral calculations for deformable drops is dynamical mesh degradation, namely if the collocation nodes are simply advected with the fluid velocity, or with the surface normal velocity, an initially regular unstructured mesh of triangles on a surface becomes highly irregular and invalid after a short simulation time. 'Passive mesh stabilization' (Zinchenko *et al.* 1997, 1999) is a family of methods to prevent mesh degradation by constructing an additional global tangential field on each surface S_α separately from the solution of a variational problem. In the present version, at any instant of time, the vertex velocities $\boldsymbol{V}_i = \mathrm{d}\boldsymbol{x}_i/\mathrm{d}t$ to be used in the shape updates are required to minimize

$$F = \sum_{\boldsymbol{x}_{ij}} \frac{1}{||\boldsymbol{x}_{ij}||^4} \left[\frac{\mathrm{d}}{\mathrm{d}t}||\boldsymbol{x}_{ij}||^2\right]^2 + \alpha \sum_{\triangle} \frac{1}{C_\triangle^2} \left(\frac{\mathrm{d}C_\triangle}{\mathrm{d}t}\right)^2 \tag{A 1}$$

under the constraints $\boldsymbol{V}_i \cdot \boldsymbol{n}(\boldsymbol{x}_i) = q_i$, where the normal velocities $q_i = \boldsymbol{u}(\boldsymbol{x}_i) \cdot \boldsymbol{n}(\boldsymbol{x}_i)$ are given by the solution of the boundary-integral equations. The summations in (A 1) are over all mesh edges $\boldsymbol{x}_{ij} = \boldsymbol{x}_j - \boldsymbol{x}_i$ (with $i < j$) on S_α and over all mesh triangles $\triangle$ on S_α,

$$C_\triangle = S_\triangle/(a^2 + b^2 + c^2) \tag{A 2}$$

is the 'compactness' of triangle $\triangle$ with area $S_\triangle$ and sides a, b, and c, and $\alpha = O(1)$ is a numerical factor set to 2 in the present calculations. The first term in (A 1) prevents the internode distances from becoming irregular in long-time simulations (as in the simplest passive mesh stabilization scheme of Zinchenko *et al.* 1997), while the second term in (A 1) resists mesh triangle degeneration and extends mesh quality to larger deformations. By the chain rule, F can be expressed as a quadratic function of $\{\boldsymbol{V}_i\}$ and minimized by conjugate gradient iterations (Zinchenko *et al.* 1997). The minimization process terminates once $F^\nu - F^{\nu+1} < \delta F^{\nu+1}$ for two successive iterations F^ν and $F^{\nu+1}$, with δ typically set to 10^{-5}. The main difference of (A 1) from the minimizing function (5.1) of paper I is the absence of curvature adaptation in (A 1), which was justified in the present calculations with not too large deformations. This simplification greatly speeds up passive mesh stabilization; additional expenses in minimizing (A 1) for all drops S_α are less than 5–6% even for $\lambda = 1$.

Appendix B. The far-field part

To facilitate calculations of the derivatives $\partial_{n+\nu,m+\mu}\, g_{k\ell}(\boldsymbol{R}_{\gamma\delta})$ etc. in (4.14)–(4.15) at each time step, it is helpful to introduce an auxiliary Green function $\boldsymbol{G}_2(\boldsymbol{x})$ and the

corresponding pressure $\boldsymbol{q}_2(\boldsymbol{x})$:

$$\boldsymbol{G}_1(\boldsymbol{x}) = \sum_{0<k_1^2+k_2^2+k_3^2\leqslant 3} \boldsymbol{G}_0(\boldsymbol{x}-\boldsymbol{P}(\boldsymbol{k})) + \boldsymbol{G}_2(\boldsymbol{x}), \tag{B 1a}$$

$$\boldsymbol{q}_1(\boldsymbol{x}) = \sum_{0<k_1^2+k_2^2+k_3^2\leqslant 3} \boldsymbol{q}_0(\boldsymbol{x}-\boldsymbol{P}(\boldsymbol{k})) + \boldsymbol{q}_2(\boldsymbol{x}). \tag{B 1b}$$

Here, $\boldsymbol{P}(\boldsymbol{k}) = k_1\boldsymbol{e}_1 + k_2\boldsymbol{e}_2 + k_3\boldsymbol{e}_3$ is a lattice point with integer k_i. Since $\boldsymbol{G}_2$ and $\boldsymbol{q}_2$ are obtained from $\boldsymbol{G}(\boldsymbol{x})$ and $\boldsymbol{q}(\boldsymbol{x})$ by subtracting the free-space contributions from the first 27 images $|k_i| \leqslant 1$, these functions are very smooth in the periodic cell V: $\{\boldsymbol{x} = \xi^1\boldsymbol{e}_1 + \xi^2\boldsymbol{e}_2 + \xi^3\boldsymbol{e}_3,\ |\xi^i| \leqslant 1/2\}$. The derivatives $\partial_{n,m}\boldsymbol{G}_2(\boldsymbol{x})$ and $\partial_{n,m}\boldsymbol{q}_2(\boldsymbol{x})$ are tabulated at each time step to a sufficient order $n_{\mathrm{tab}}(n_1, n_2, n_3)$ on a mesh $\boldsymbol{x} = hn_1\boldsymbol{e}_1 + hn_2\boldsymbol{e}_2 + hn_3\boldsymbol{e}_3$, with $h = 0.5/N_T$ and the integers n_i in the range $-N_T \leqslant n_1 \leqslant N_T$, $0 \leqslant n_2, n_3 \leqslant N_T$; due to smoothness of $\boldsymbol{G}_2$ and $\boldsymbol{q}_2$, small values of $N_T = 6$–7 sufficed for all applications, even for a high order of n_{tab}. Fast tabulation of $\partial_{n,m}\boldsymbol{G}_2$ and $\partial_{n,m}\boldsymbol{q}_2$ is based on Ewald-like forms:

$$\begin{aligned}\boldsymbol{G}(\boldsymbol{x}) = {} & \frac{\boldsymbol{I}}{4\pi D^{1/2}} \\ & -\frac{1}{4\pi^{3/2}}\sum_{\boldsymbol{k}}\int_{\pi^{1/2}}^{\infty}\exp\{-t^2[\boldsymbol{x}-\boldsymbol{P}(\boldsymbol{k})]^2\}\{\boldsymbol{I} + 2t^2[\boldsymbol{x}-\boldsymbol{P}(\boldsymbol{k})][\boldsymbol{x}-\boldsymbol{P}(\boldsymbol{k})]\}\,\mathrm{d}t \\ & -\frac{1}{4\pi^2 D^{1/2}}{\sum_{\boldsymbol{k}}}'\left\{\boldsymbol{I} - \pi\boldsymbol{Q}(\boldsymbol{k})\boldsymbol{Q}(\boldsymbol{k})\left[1 + \frac{1}{\pi\boldsymbol{Q}^2(\boldsymbol{k})}\right]\right\}\frac{\exp\left[-\pi\boldsymbol{Q}^2(\boldsymbol{k}) - 2\pi\mathrm{i}\boldsymbol{Q}(\boldsymbol{k})\cdot\boldsymbol{x}\right]}{\boldsymbol{Q}^2(\boldsymbol{k})},\end{aligned} \tag{B 2a}$$

$$\begin{aligned}\boldsymbol{q}(\boldsymbol{x}) = {} & -\frac{\boldsymbol{x}}{D^{1/2}} - \frac{1}{\pi^{3/2}}\sum_{\boldsymbol{k}}[\boldsymbol{x}-\boldsymbol{P}(\boldsymbol{k})]\int_{\pi^{1/2}}^{\infty}\exp\{-t^2[\boldsymbol{x}-\boldsymbol{P}(\boldsymbol{k})]^2\}t^2\,\mathrm{d}t \\ & -\frac{\mathrm{i}}{2\pi D^{1/2}}{\sum_{\boldsymbol{k}}}'\frac{\boldsymbol{Q}(\boldsymbol{k})\exp\left[-\pi\boldsymbol{Q}^2(\boldsymbol{k}) - 2\pi\mathrm{i}\boldsymbol{Q}(\boldsymbol{k})\cdot\boldsymbol{x}\right]}{\boldsymbol{Q}^2(\boldsymbol{k})}.\end{aligned} \tag{B 2b}$$

The first sums in (B 2a, b) are over all lattice points $\boldsymbol{P}(\boldsymbol{k})$ in the physical space, the second sums are over the reciprocal (wave-space) lattice points $\boldsymbol{Q}(\boldsymbol{k}) = k_1\boldsymbol{E}^1 + k_2\boldsymbol{E}^2 + k_3\boldsymbol{E}^3$ (where $\boldsymbol{E}^i$ is the basis contravariant to $\boldsymbol{e}_i$ and k_i are integers) excluding $k_1 = k_2 = k_3 = 0$; a constant has been added to zero the average of $\boldsymbol{G}$ over a periodic cell. For a particular lattice (2.1), $\boldsymbol{E}^1 = \boldsymbol{e}_1 - \gamma\boldsymbol{e}_2^o$, $\boldsymbol{E}^2 = \boldsymbol{e}_2^o$, $\boldsymbol{E}^3 = \boldsymbol{e}_3^o$ and $D = \det||\boldsymbol{e}_i\cdot\boldsymbol{e}_j|| = 1$. Expressions (B 2) follow from Hasimoto (1959); Beenakker's (1986) approach, although popular, gives slower convergent and more cumbersome series less amenable in calculating high-order derivatives. To obtain Ewald-like forms for $\boldsymbol{G}_2$ and $\boldsymbol{q}_2$, the upper integration limits in (B 2a, b) are replaced by zero for $k_1^2+k_2^2+k_3^2 \leqslant 3$. Using special algebraic properties of (B 2a, b) and joining contributions from physical and wave spaces, calculations of $\partial_{n,m}\boldsymbol{G}_2(\boldsymbol{x})$ and $\partial_{n,m}\boldsymbol{q}_2(\boldsymbol{x})$ to order n_{tab} can be made in $\approx 13\ n_{\mathrm{tab}}^2$ real floating point multiplications per lattice point and do not require standard error or complementary error functions (Appendix C); for a typical number of lattice points $\sim$ 170–180 in each sum (B 2a–b) and $n_{\mathrm{tab}} = 10$, $N_T = 6$, tabulation of $\partial_{n,m}\boldsymbol{G}_2(\boldsymbol{x})$ and $\partial_{n,m}\boldsymbol{q}_2(\boldsymbol{x})$ takes only about 4 s on a DEC 600au workstation.

To evaluate $\partial_{n,m}\mathbf{G}_1(\boldsymbol{R}_{\gamma\delta})$ and $\partial_{n,m}\boldsymbol{q}_1(\boldsymbol{R}_{\gamma\delta})$, the minimal vector $\boldsymbol{R}_{\gamma\delta}$ is shifted periodically to the new position $\boldsymbol{R}^*_{\gamma\delta} \in V$ (usually $\boldsymbol{R}^*_{\gamma\delta} = \boldsymbol{R}_{\gamma\delta}$). Obviously,

$$\mathbf{G}_1\left(\boldsymbol{R}_{\gamma\delta}\right) = \sum_{0\leqslant k_1^2+k_2^2+k_3^2\leqslant 3}{}' \mathbf{G}_o(\boldsymbol{R}^*_{\gamma\delta} - \boldsymbol{P}(\boldsymbol{k})) + \mathbf{G}_2(\boldsymbol{R}^*_{\gamma\delta}), \tag{B 3a}$$

$$\boldsymbol{q}_1(\boldsymbol{R}_{\gamma\delta}) = \sum_{0\leqslant k_1^2+k_2^2+k_3^2\leqslant 3}{}' \boldsymbol{q}_o(\boldsymbol{R}^*_{\gamma\delta} - \boldsymbol{P}(\boldsymbol{k})) + \boldsymbol{q}_2(\boldsymbol{R}^*_{\gamma\delta}), \tag{B 3b}$$

where the terms (k_1, k_2, k_3) with $\boldsymbol{R}^*_{\gamma\delta} - \boldsymbol{P}(\boldsymbol{k}) = \boldsymbol{R}_{\gamma\delta}$ are excluded from the summations. The derivatives $\partial_{n,m}\mathbf{G}_o(\boldsymbol{R}^*_{\gamma\delta} - \boldsymbol{P}(\boldsymbol{k}))$ and $\partial_{n,m}\boldsymbol{q}_o(\boldsymbol{R}^*_{\gamma\delta} - \boldsymbol{P}(\boldsymbol{k}))$ are calculated directly by a special technique at a cost of only $\approx 3.5\, n_{\text{tab}}^2$ real floating point multiplications for each of 26 images in the sums (B 3*a*, *b*) (Appendix D). Additional terms $\partial_{n,m}\mathbf{G}_2(\boldsymbol{R}^*_{\gamma\delta})$ and $\partial_{n,m}\boldsymbol{q}_2(\boldsymbol{R}^*_{\gamma\delta})$ are evaluated by the symmetry properties of $\mathbf{G}_2$ and $\boldsymbol{q}_2$ and table interpolation: the vector $\boldsymbol{R}^*_{\gamma\delta} = \xi^i \boldsymbol{e}_i$ is mapped onto a new position $\boldsymbol{R}^{**}_{\gamma\delta}$ in the tabulated region $|\xi^1| \leqslant 1/2$, $0 \leqslant \xi^2, \xi^3 \leqslant 1/2$ by $\boldsymbol{x} \leftarrow -\boldsymbol{x}$ and/or $\xi^3 \leftarrow -\xi^3$ transformations, and second- or third-order Taylor expansions from the node $\boldsymbol{x}_o$ nearest to $\boldsymbol{R}^{**}_{\gamma\delta}$ is used (cf. (3.81) of paper I):

$$\partial_{n,m}\left[\mathbf{G}_2(\boldsymbol{x}) - \tfrac{1}{2}\boldsymbol{q}_2(\boldsymbol{x})\boldsymbol{x}\right]_{\boldsymbol{x}=\boldsymbol{R}^*_{\gamma\delta}}$$

$$= \sum_{v\leqslant v_E}\sum_{\mu=-v}^{v} \partial_{n+v,m+\mu}[\mathbf{G}_2(\boldsymbol{x}) - \tfrac{1}{2}\boldsymbol{q}_2(\boldsymbol{x})\boldsymbol{x}]_{\boldsymbol{x}=\boldsymbol{x}_o} Z_{v,\mu}(\boldsymbol{R}^{**}_{\gamma\delta} - \boldsymbol{x}_o), \tag{B 4a}$$

$$\partial_{n,m}\boldsymbol{q}_2\left(\boldsymbol{R}^*_{\gamma\delta}\right) = \sum_{v\leqslant v_E}\sum_{\mu=-v}^{v} \partial_{n+v,m+\mu}\boldsymbol{q}_2(\boldsymbol{R}^*_{\gamma\delta}) Z_{v,\mu}(\boldsymbol{R}^{**}_{\gamma\delta} - \boldsymbol{x}_o) \tag{B 4b}$$

(where $v_E = 2$ or 3), which completes the task of calculating the derivatives in (4.14).

When $\lambda \neq 1$, the necessary derivatives of the stresslet $t_{ks\ell}$ and of the associated pressure $\tilde{q}_1^{(k,s)}$ in (4.15) can be expressed via $\partial_{v',\mu'}\boldsymbol{g}(\boldsymbol{R}_{\gamma\delta})$ and $\partial_{v',\mu'}\boldsymbol{q}_1(\boldsymbol{R}_{\gamma\delta})$ (see paper I):

$$\partial_{v,\mu}\tilde{q}_1^{(1,s)} = (\partial_{v+1,\mu+1} - \partial_{v+1,\mu-1})q_1^{(s)}, \tag{B 5a}$$

$$\partial_{v,\mu}\tilde{q}_1^{(2,s)} = \mathrm{i}(\partial_{v+1,\mu+1} + \partial_{v+1,\mu-1})q_1^{(s)}, \tag{B 5b}$$

$$\partial_{v,\mu}\tilde{q}_1^{(3,s)} = 2\partial_{v+1,\mu}q_1^{(s)}, \tag{B 5c}$$

$$\partial_{v,\mu}t_{ks\ell}(\boldsymbol{x}) = -\delta_{ks}\partial_{v,\mu}q_1^{(\ell)} + \tfrac{1}{2}\delta_{k\ell}\partial_{v,\mu}q_1^{(s)} + \tfrac{1}{2}\delta_{s\ell}\partial_{v,\mu}q_1^{(k)}$$
$$+\partial_{v,\mu}D_k g_{s\ell} + \partial_{v,\mu}D_s g_{k\ell} - \delta_{ks}\partial_{v,\mu}x_\ell, \tag{B 5d}$$

$$\partial_{v,\mu}D_1 g_{s\ell} = \tfrac{1}{2}[\partial_{v+1,\mu+1} - \partial_{v+1,\mu-1}]g_{s\ell}, \tag{B 6a}$$

$$\partial_{v,\mu}D_2 g_{s\ell} = \tfrac{1}{2}\mathrm{i}[\partial_{v+1,\mu+1} + \partial_{v+1,\mu-1}]g_{s\ell}, \tag{B 6b}$$

$$\partial_{v,\mu}D_3 g_{s\ell} = \partial_{v+1,\mu}g_{s\ell}. \tag{B 6c}$$

The far-field truncation bounds $v + n \leqslant v^*_{ff}(\delta, \gamma)$ for (4.14), $v + n \leqslant \tilde{v}^*_{ff}$ for (4.15) and the order of interpolation v_E allow one to determine the necessary order n_{tab} (n_1, n_2, n_3) of tabulating the derivatives $\partial_{n,m}\mathbf{G}_2$ and $\partial_{n,m}\boldsymbol{q}_2$ for every mesh point (n_1, n_2, n_3).

Although (4.15) can be used directly to accumulate contributions of all blocks $\mathscr{B}_\gamma \notin$

$S_\alpha \ni \boldsymbol{y}$ to the coefficients before $Z_{n,m}(\boldsymbol{R}_\delta)$ and $\boldsymbol{R}_\delta Z_{n,m}(\boldsymbol{R}_\delta)$ for pointwise calculations, it is more advantageous to transform (4.15) first to a more efficient form. Substituting (B 5)–(B 6) into (4.15) yields

$$\sum_{\nu=0}^{\infty}\sum_{\mu=-\nu}^{\nu}\left[\tilde{D}^{(\gamma)}_{\nu,\mu,k,s}\partial_{n+\nu,m+\mu}t_{ks\ell}(\boldsymbol{R}_{\gamma\delta})+\tfrac{1}{2}\tilde{E}_{\nu,\mu,k,s,\ell}\partial_{n+\nu,m+\mu}\tilde{q}_1^{(ks)}(\boldsymbol{R}_{\gamma\delta})\right]$$

$$=\sum_{\nu=0}^{\infty}\sum_{\mu=-\nu}^{\nu}\{\hat{E}^{(\gamma)}_{\nu,\mu,k,\ell}\partial_{n+\nu,m+\mu}q_1^{(k)}(\boldsymbol{R}_{\gamma\delta})+\hat{D}^{(\gamma)}_{\nu,\mu,k}\partial_{n+\nu,m+\mu}g_{k\ell}(\boldsymbol{R}_{\gamma\delta})$$

$$-\tilde{D}_{\nu,\mu,k,k}\partial_{n+\nu,m+\mu}[q_1^{(\ell)}(\boldsymbol{R}_{\gamma\delta})+(R_{\gamma\delta})_\ell]\} \tag{B 7}$$

and

$$\sum_{\nu=0}^{\infty}\sum_{\mu=-\nu}^{\nu}\tilde{D}^{(\gamma)}_{\nu,\mu,k,s}\partial_{n+\nu,m+\mu}\tilde{q}_1^{(ks)}(\boldsymbol{R}_{\gamma\delta})=\sum_{\nu=0}^{\infty}\sum_{\mu=-\nu}^{\nu}\hat{D}^{(\gamma)}_{\nu,\mu,k}\partial_{n+\nu,m+\mu}q_1^{(k)}(\boldsymbol{R}_{\gamma\delta}), \tag{B 8}$$

where

$$\hat{E}^{(\gamma)}_{\nu,\mu,k,\ell}=\tfrac{1}{2}(\tilde{E}_{\nu-1,\mu-1,1,k,\ell}+\mathrm{i}\tilde{E}^{(\gamma)}_{\nu-1,\mu-1,2,k,\ell}-\tilde{E}^{(\gamma)}_{\nu-1,\mu+1,1,k,\ell}$$

$$+\mathrm{i}\tilde{E}^{(\gamma)}_{\nu-1,\mu+1,2,k,\ell})+\tilde{E}^{(\gamma)}_{\nu-1,\mu,3,k,\ell}+\tilde{D}^{(\gamma)}_{\nu,\mu,\ell,k} \tag{B 9}$$

and

$$\hat{D}^{(\gamma)}_{\nu,\mu,k}=\tilde{D}^{(\gamma)}_{\nu-1,\mu-1,1,k}+\mathrm{i}\tilde{D}^{(\gamma)}_{\nu-1,\mu-1,2,k}-\tilde{D}^{(\gamma)}_{\nu-1,\mu+1,1,k}+\mathrm{i}\tilde{D}^{(\gamma)}_{\nu-1,\mu+1,2,k}+2\tilde{D}^{(\gamma)}_{\nu-1,\mu,3,k} \tag{B 10}$$

(assuming that $\tilde{E}^{(\gamma)}_{\nu',\mu'}$ and $\tilde{D}^{(\gamma)}_{\nu',\mu'}$ are non-zero only for $|\mu'|\leqslant\nu'$). The new $\hat{E}-$ and $\hat{D}-$ coefficients are precalculated for each block on every iteration. This improvement of (4.15) (overlooked in paper I) speeds up the far-field part of the double-layer calculations about two-fold.

For very large systems (several hundred drops and more), only low-order derivatives of $\mathbf{G}_1$ and $\boldsymbol{q}_1$ suffice, so it is unnecessary to subtract the contributions of 26 images $0<k_1^2+k_2^2+k_3^2\leqslant 3$ in (B 1), which would further accelerate the far-field part of the code. Besides, for very large N, it is advantageous to disable drop partitioning into blocks, even for relatively strong deformations. It turns out, after all optimizations, that the far-field part with $O(N^2)$ scaling is fast compared to the rest of the code, and the whole algorithm scales practically linearly in N, as long as $N<1000$ (assuming that $N_\triangle=O(10^3)$ boundary elements per drop are used). Only for $N\gg 1000$, would a quadratic scaling of the present algorithm be pronounced. However, regardless of the method, it may not be possible to dynamically simulate such large concentrated systems of deformable three-dimensional drops with adequate resolution $N_\triangle\sim 10^3$ on present-day computers. For this reason, other approaches designed to rigorously eliminate the $O(N^2)$ scaling, in particular, the FMM scheme (e.g. Greengard & Rokhlin 1997; Sangani & Mo 1996; Popov & Power 2001) were not incorporated in our algorithm.

Appendix C. Fast differentiation of Ewald-like forms

Let

$$S^{\mu}_{p,\nu}(\boldsymbol{x})=\sum_{\boldsymbol{k}}{}'|\boldsymbol{Q}(\boldsymbol{k})|^p(Q_1-\mathrm{i}Q_2)^\mu Q_3^{\nu-\mu}\exp[-\pi\boldsymbol{Q}^2(\boldsymbol{k})-2\pi\mathrm{i}\boldsymbol{Q}(\boldsymbol{k})\cdot\boldsymbol{x}] \tag{C 1}$$

for $\mu \geqslant 0$ and $S^{\mu}_{p,v}(\boldsymbol{x}) = (-1)^{\mu}\overline{S}^{-\mu}_{p,v}(-\boldsymbol{x})$ for $\mu < 0$, where for brevity, $\boldsymbol{Q}(\boldsymbol{k}) = (Q_1,\ Q_2,\ Q_3)$ in Cartesian coordinates. An economical direct way of calculating all the derivatives $\partial_{v,\mu}$ of the wave-space parts of Green's function (B 2*a*) and pressure (B 2*b*) to order $v = n_{\mathrm{tab}}$ for a given $\boldsymbol{x}$ is to compute first the lattice sums (C1):

$$\left.\begin{array}{lll} S^{\mu}_{-4,v}, S^{\mu}_{-2,v} & \text{for} & 0 \leqslant \mu \leqslant v \leqslant n_{\mathrm{tab}} + 2, \\ S^{\mu}_{0,v} & \text{for} & 0 \leqslant \mu \leqslant v \leqslant n_{\mathrm{tab}}, \\ S^{\mu}_{2,v} & \text{for} & 0 \leqslant \mu \leqslant v \leqslant n_{\mathrm{tab}} - 2, \end{array}\right\} \tag{C 2}$$

at a $O(n^2_{\mathrm{tab}})$-cost per lattice point, and additional sums

$$\left.\begin{array}{lll} S^{-1}_{-4,v},\ S^{-1}_{-2,v} & \text{for} & 1 \leqslant v \leqslant n_{\mathrm{tab}} + 2, \\ S^{-1}_{0,v} & \text{for} & 1 \leqslant v \leqslant n_{\mathrm{tab}}, \\ S^{-2}_{-4,v},\ S^{-2}_{-2,v} & \text{for} & 2 \leqslant v \leqslant n_{\mathrm{tab}} + 2, \end{array}\right\} \tag{C 3}$$

at a $O(n_{\mathrm{tab}})$-cost per lattice point. Since

$$\partial_{v,\mu} \exp[-2\pi \mathrm{i}\boldsymbol{Q}(\boldsymbol{k}) \cdot \boldsymbol{x}] = (-2\pi \mathrm{i})^{v}(Q_1 - \mathrm{i}Q_2)^{\mu} Q_3^{v-\mu} \exp[-2\pi \mathrm{i}\boldsymbol{Q}(\boldsymbol{k}) \cdot \boldsymbol{x}], \tag{C 4}$$

all the necessary derivatives of the wave-space parts of (B 2*a*, *b*) can be expressed in terms of (C2)–(C3). For example, the product Q_1Q_2 in (B 2*a*) is handled for $\mu \geqslant 2$ as

$$\begin{aligned} Q_1Q_2(Q_1 - \mathrm{i}Q_2)^{\mu} Q_3^{v-\mu} &= -\frac{\mathrm{i}}{4}[(Q_1 + \mathrm{i}Q_2)^2 - (Q_1 - \mathrm{i}Q_2)^2](Q_1 - \mathrm{i}Q_2)^{\mu} Q_3^{v-\mu} \\ &= -\frac{\mathrm{i}}{4}\{[\boldsymbol{Q}^2(\boldsymbol{k}) - Q_3^2](Q_1 - \mathrm{i}Q_2)^{\mu-2} Q_3^{v-\mu} - (Q_1 - \mathrm{i}Q_2)^{\mu+2} Q_3^{v-\mu}\}. \end{aligned} \tag{C 5}$$

By expressing Q_1 and Q_2 via $Q_1 + \mathrm{i}Q_2$ and $Q_1 - \mathrm{i}Q_2$, similar transformations are applied to other products $Q_jQ_m(Q_1 - \mathrm{i}Q_2)^{\mu} Q_3^{v-\mu}$ and $Q_j(Q_1 - \mathrm{i}Q_2)^{\mu} Q_3^{v-\mu}$. Also, the calculations of (C1) are accelerated by factorizing the exponents (cf. Zinchenko 1994).

For calculating the derivatives $\partial_{v,\mu}$ of the physical-space contributions to G_2 and $\boldsymbol{q}_2$ to order $v = n_{\mathrm{tab}}$, it is sufficient to compute the lattice sums

$$\left.\begin{array}{lll} \displaystyle\sum_{\boldsymbol{k}} (y_1 - \mathrm{i}y_2)^{\mu} J^{\mu}_{v} & \text{for } 0 \leqslant \mu \leqslant v \leqslant n_{\mathrm{tab}} + 1, & \\ \displaystyle\sum_{\boldsymbol{k}} (y_1 - \mathrm{i}y_2)^{\mu} J^{\mu}_{v} P_m(\boldsymbol{k}) & \text{for } 0 \leqslant \mu \leqslant v \leqslant n_{\mathrm{tab}} + 1, & m = 1, 2, 3, \\ \displaystyle\sum_{\boldsymbol{k}} [(y_1 - \mathrm{i}y_2)^{\mu} J^{\mu+1}_{v+1} y_2 + \mathrm{i}\mu(y_1 - \mathrm{i}y_2)^{\mu-1} J^{\mu}_{v}] & \text{for } 0 \leqslant \mu \leqslant v \leqslant n_{\mathrm{tab}}, & \\ \displaystyle\sum_{\boldsymbol{k}} [(y_1 - \mathrm{i}y_2)^{\mu} J^{\mu+1}_{v+1} y_2 + \mathrm{i}\mu(y_1 - \mathrm{i}y_2)^{\mu-1} J^{\mu}_{v}] P_m(\boldsymbol{k}) & \text{for } 0 \leqslant \mu \leqslant v \leqslant n_{\mathrm{tab}}, & m = 1, 2. \end{array}\right\} \tag{C 6}$$

Here, for brevity, $\boldsymbol{y} = \boldsymbol{x} - \boldsymbol{P}(\boldsymbol{k})$, indices 1, 2, and 3 denote Cartesian coordinates, and

$$J^{\mu}_{v} = \frac{2^{\mu+1}}{\pi^{1/2}} \int t^{v+\mu} H_{v-\mu}(y_3 t) \exp(-t^2 \boldsymbol{y}^2)\, \mathrm{d}t, \tag{C 7}$$

with $H_n(\xi)$ being the Hermite polynomial of degree n; integrations in (B 7) and below are performed from $\pi^{1/2}$ to ∞ for $k_1^2 + k_2^2 + k_3^2 > 3$ and from $\pi^{1/2}$ to zero otherwise.

Recurrent relations (Zinchenko 1994)

$$J_{v+1}^{v+1} = \frac{1}{\boldsymbol{y}^2}[2(2\pi)^v \exp(-\pi\boldsymbol{y}^2) + (2v+1)J_v^v], \quad J_{v+1}^{\mu} = y_3 J_{v+1}^{\mu+1} - (v-\mu)J_v^{\mu+1}, \tag{C 8}$$

are applied for fast calculation of J_v^μ at $\boldsymbol{y} \neq 0$; for J_o^o at $k_1^2 + k_2^2 + k_3^2 > 3$, expensive computation of the complementary error function is avoided altogether by factoring out $\exp(-\pi\boldsymbol{y}^2)/(\pi\boldsymbol{y}^2)$ and pretabulating the smooth remaining part (Zinchenko 1994).

To link the derivatives $\partial_{v,\mu}$ of the physical-space parts of $\mathbf{G}_2$ and $\boldsymbol{q}_2$ to the lattice sums (C 6), we note that

$$(G_2)_{nm}(\boldsymbol{x}) - \tfrac{1}{2}(q_2)_n(\boldsymbol{x})x_m = -\frac{1}{4\pi^{3/2}}\sum_{\boldsymbol{k}}\int \exp(-t^2\boldsymbol{y}^2)[\delta_{nm} - 2t^2 y_n P_m(\boldsymbol{k})]\,\mathrm{d}t + \cdots, \tag{C 9}$$

where only integral contributions are shown. Using (3.76) of paper I yields

$$\left.\begin{aligned}
\partial_{v,\mu}\int \exp(-t^2\boldsymbol{y}^2)\,\mathrm{d}t &= \frac{\pi^{1/2}}{2}(-1)^v(y_1 - \mathrm{i}y_2)^\mu J_v^\mu,\\
\partial_{v,\mu}(y_2\int t^2\exp(-t^2\boldsymbol{y}^2)\,\mathrm{d}t) &= \frac{\pi^{1/2}}{4}(-1)^v[(y_1 - \mathrm{i}y_2)^\mu y_2 J_{v+1}^{\mu+1} + \mathrm{i}\mu(y_1 - \mathrm{i}y_2)^{\mu-1}J_v^\mu],\\
\partial_{v,\mu}(y_3\int t^2\exp(-t^2\boldsymbol{y}^2)\,\mathrm{d}t) &= \frac{\pi^{1/2}}{4}(-1)^v(y_1 - \mathrm{i}y_2)^\mu J_{v+1}^\mu,\\
\partial_{v,\mu}[(y_1 - \mathrm{i}y_2)\int t^2\exp(-t^2\boldsymbol{y}^2)\,\mathrm{d}t] &= \frac{\pi^{1/2}}{4}(-1)^v(y_1 - \mathrm{i}y_2)^{\mu+1}J_{v+1}^{\mu+1}.
\end{aligned}\right\} \tag{C 10}$$

Since $\mathbf{G}_2$ is a symmetric tensor, the lattice sums (C 6) and relations (C 10) allow all the derivatives $\partial_{v,\mu}$ of the physical-space parts of $\mathbf{G}_2$ and $\boldsymbol{q}_2$ to be calculated.

Appendix D. Fast differentiation of free-space Green functions

To calculate the derivatives $\partial_{v,\mu}$ of the sums (B 3*a*, *b*) to order $v = v_{\max}$, it is sufficient to compute the lattice sums

$$\sum_{0\leqslant k_1^2+k_2^2+k_3^2\leqslant 3}{}' U_v^\mu(\boldsymbol{x} - \boldsymbol{P}(\boldsymbol{k})), \quad 0 \leqslant \mu \leqslant v \leqslant v_{\max}+1, \tag{D 1a}$$

$$\sum_{0\leqslant k_1^2+k_2^2+k_3^2\leqslant 3}{}' [\boldsymbol{x} - \boldsymbol{P}(\boldsymbol{k})]^2 U_v^\mu(\boldsymbol{x} - \boldsymbol{P}(\boldsymbol{k})), \quad 0 \leqslant \mu \leqslant v \leqslant v_{\max}+2, \tag{D 1b}$$

where

$$U_v^\mu(\boldsymbol{r}) = (D_1 - \mathrm{i}D_2)^\mu D_3^{v-\mu}\left(\frac{1}{r}\right), \quad D_i = \frac{\partial}{\partial r_i}. \tag{D 2}$$

Fast computations of (D 1*a*, *b*) are performed through recurrent relations:

$$U_j^j = -(2j-1)\frac{(r_1 - \mathrm{i}r_2)}{r^2}U_{j-1}^{j-1}, \quad U_j^\mu = -(2j-1)\frac{r_3}{r^2}U_{j-1}^\mu - \frac{[(j-1)^2 - \mu^2]}{r^2}U_{j-2}^\mu. \tag{D 3}$$

We also note that

$$\begin{aligned}
-8\pi\partial_{v,\mu}(G_o)_{km}(\boldsymbol{r}) = {}& \delta_{k,m}\partial_{v,\mu}\left(\frac{1}{r}\right) - r_m\partial_{v,\mu}D_k\left(\frac{1}{r}\right)\\
& -\mu(\delta_{m,1} - \mathrm{i}\delta_{m,2})\partial_{v-1,\mu-1}D_k\left(\frac{1}{r}\right) - (v-\mu)\delta_{3,m}\partial_{v-1,\mu}D_k\left(\frac{1}{r}\right)
\end{aligned} \tag{D 4}$$

and $\partial_{v,\mu}\boldsymbol{q}_o(\boldsymbol{r}) = (4\pi)^{-1}\partial_{v,\mu}\nabla(1/r)$. Expressing D_1 and D_2 via $D_1 + \mathrm{i}D_2$, $D_1 - \mathrm{i}D_2$ and using harmonicity of $1/r$, all the derivatives $\partial_{v,\mu}$ of the sums (B $3a,b$) can be linked to the lattice sums (D $1a,b$).

REFERENCES

Astarita, G. & Marrucci, G. 1974 *Principles of Non-Newtonian Fluid Mechanics*. McGraw-Hill.

Barthès-Biesel, D. & Acrivos, A. 1973 The rheology of suspensions and its relation to phenomenological theories for non-Newtonian fluids. *Intl J. Multiphase Flow* **1**, 1–24.

Beenakker, C. W. J. 1986 Ewald sum of the Rotne–Prager tensor. *J. Chem. Phys.* **85**, 1581.

Breyiannis, G. & Pozrikidis, C. 2000 Simple shear flow of elastic capsules. *Theor. Comput. Fluid Dyn.* **13**, 327–347.

Charles, R. & Pozrikidis, C. 1998 Significance of the dispersed-phase viscosity on the simple shear flow of suspensions of two-dimensional drops. *J. Fluid Mech.* **365**, 205–234.

Cox, R. G. 1969 The deformation of a drop in a general time-dependent fluid flow. *J. Fluid Mech.* **37**, 601–623.

Frankel, N. A. & Acrivos, A. 1970 The constitutive equation for a dilute emulsion. *J. Fluid Mech.* **44**, 65–78.

Greengard, L. & Rokhlin, V. 1997 A new version of the fast multipole method for the Laplace equation in three dimensions. *Acta Numer.* **6**, 229–269.

Hansen, J. P. & McDonald, I. R. 1976 *Theory of Simple Liquids* Academic.

Hasimoto, H. 1959 On the periodic fundamental solutions of the Stokes equations and their application to viscous flow past a cubic array of spheres. *J. Fluid Mech.* **5**, 317–328.

Kennedy, M. R., Pozrikidis, C. & Skalak, R. 1994 Motion and deformation of liquid drops, and the rheology of dilute emulsions in simple shear flow. *Comput. Fluids* **23**, 251–278.

Kim, S. & Karilla, S. 1991 *Microhydrodynamics: Principles and Selected Applications*. Butterworth–Heinemann.

Kushch, V. I. & Sangani, A. S. 2000*a* Conductivity of a composite containing uniformly oriented penny-shaped cracks or perfectly conducting disks. *Proc. R. Soc. Lond.* A **456**, 683–699.

Kushch, V. I. & Sangani, A. S. 2000*b* Stress intensity factor and effective stiffness of a solid containing aligned penny-shaped cracks. *Intl J. Solids Structures* **37**, 6555.

Li, X., Charles, R. & Pozrikidis, C. 1996 Simple shear flow of suspensions of liquid drops. *J. Fluid Mech.* **320**, 395–416.

Li, X. & Pozrikidis, C. 2000 Wall-bounded shear flow and channel flow of suspensions of liquid drops. *Intl J. Multiphase Flow* **26**, 1247–1279.

Loewenberg, M. 1998 Numerical simulation of concentrated emulsion flows. *Trans. ASME: J. Fluids Engng* **120**, 824–832.

Loewenberg, M. & Hinch, E. J. 1996 Numerical simulation of a concentrated emulsion in shear flow. *J. Fluid Mech.* **321**, 395–419.

MacKeown, P. K. 1997 *Stochastic Simulation in Physics*. Springer.

Mo, G. & Sangani, A. S. 1994 A method for computing Stokes flow interactions among spherical objects and its application to suspensions of drops and porous particles. *Phys. Fluids* **6**, 1637–1652.

Popov, V. & Power, H. 2001 An $O(N)$ Taylor series multipole boundary element method for three-dimensional elasticity problems. *Eng. Anal. with Boundary Elements* **25**, 7–18.

Pozrikidis, C. 1992 *Boundary Integral and Singularity Methods for Linearized Viscous Flow*. Cambridge University Press.

Pozrikidis, C. 1993 On the transient motion of ordered suspensions of liquid drops. *J. Fluid Mech.* **246**, 301–320.

Pozrikidis, C. 2001 Interfacial dynamics for Stokes flow. *J. Comput. Phys.* **169**, 250–301.

Rallison, J. M. 1981 A numerical study of the deformation and burst of a viscous drop in general shear flows. *J. Fluid Mech.* **109**, 465–482.

Rivlin, R. S. & Ericksen, J. L. 1955 Stress-deformation relations for isotropic materials. *Arch. Rat. Mech. Anal.* **4**, 323–425.

Rother, M. A., Zinchenko, A. Z. & Davis, R. H. 2001 A three-dimensional boundary-integral

algorithm for thermocapillary-driven motion of deformable drops. *J. Colloid Interface Sci.* (submitted).

Sangani, A. S. & Lu, W. 1987 Effective viscosity of an ordered suspension of small drops. *Z. Angew. Math. Phys.* **38**, 557–572.

Sangani, A. S. & Mo, G. 1996 An $O(N)$ algorithm for Stokes and Laplace interactions of particles. *Phys. Fluids* **8**, 1990–2010.

Zhou, H. & Pozrikidis, C. 1993 The flow of ordered and random suspensions of two-dimensional drops in a channel. *J. Fluid Mech.* **255**, 103–127.

Zhou, H. & Pozrikidis, C. 1994 Pressure-driven flow of suspensions of liquid drops. *Phys. Fluids* A **6**, 80–94.

Zinchenko, A. Z. 1994 An efficient algorithm for calculating multiparticle thermal interaction in a concentrated dispersion of spheres. *J. Comput. Phys.* **111**, 120–135.

Zinchenko, A. Z. 1998 Effective conductivity of loaded granular materials by numerical simulation. *Phil. Trans. R. Soc. Lond.* A **356**, 2953–2998.

Zinchenko, A. Z. & Davis, R. H. 2000 An efficient algorithm for hydrodynamical interaction of many deformable drops. *J. Comput. Phys.* **157**, 539–587 (referred to herein as paper I).

Zinchenko, A. Z., Rother, M. A. & Davis, R. H. 1997 A novel boundary-integral algorithm for viscous interaction of deformable drops. *Phys. Fluids* **9**, 1493–1511.

Zinchenko, A. Z., Rother, M. A. & Davis, R. H. 1999 Cusping, capture and breakup of interacting drops by a curvatureless boundary-integral algorithm. *J. Fluid Mech.* **391**, 249–292.